Infrared Radiation in the Mesosphere and Lower Thermosphere: Energetic Effects and Remote Sensing

Artem G. Feofilov · Alexander A. Kutepov

Abstract This paper discusses the formation mechanisms of infrared radiation in the mesosphere and lower thermosphere (MLT), the energetic effects of the radiative absorption/emission processes, and the retrieval of atmospheric parameters from infrared radiation measurements. In the MLT and above, the vibrational levels of the molecules involved in radiative transitions are not in local thermodynamic equilibrium (LTE) with the surrounding medium, and this then requires specific theoretical treatment. The non-LTE models for CO_2, O_3, and H_2O molecules are presented, and the radiative cooling/heating rates estimated for five typical atmospheric scenarios, from polar winter to polar summer, are shown. An optimization strategy for calculating the cooling/heating rates in general circulation models is proposed, and its accuracy is estimated for CO_2. The sensitivity of the atmospheric quantities retrieved from infrared observations made from satellites to the non-LTE model parameters is shown.

1 Introduction

In this paper, we concentrate on (a) the role of the infrared (IR) radiation in the energy budget of the mesosphere and lower thermosphere (MLT) as well as (b) on the IR radiation emerging from the atmosphere, which is observed with various instruments from space. Both topics are strongly linked and require detailed consideration of formation and

A. G. Feofilov (✉)
Laboratory of Dynamical Meteorology, École Polytechnique, Palaiseau, France
e-mail: artem.feofilov@lmd.polytechnique.fr

A. A. Kutepov
The Catholic University of America, Washington, DC, USA

A. A. Kutepov
NASA Goddard Space Flight Center, Greenbelt, MD, USA

propagation of the IR radiation in the MLT and its interactions with the various components of the atmosphere.

The translational degrees of freedom of all atmospheric molecular and atomic gaseous compounds represent the heat reservoir. This reservoir obtains or loses energy due to a number of sources and sinks, among them heating and cooling related to various types of mass motions, redistribution of energy released in the course of various photochemical reactions (the translational energy, the chemical energy and the nascent electronic, vibration and rotational energy of the reaction products), and absorption and emission of the IR radiation. In the latter case, one usually speaks about the interaction between matter and the IR radiative field, which, for the case of the MLT, includes the atmospheric radiation formed in these layers, the upwelling radiation from the ground and lower atmosphere, and, during daytime, the IR solar radiation.

Our primary interest here is with the interaction of the heat reservoir and the IR radiative field. The energy exchange between them is carried out through an intermediate reservoir of vibrational and rotational energy of molecular atmospheric compounds: the photons are absorbed and emitted by molecules of optically active gases through the processes of spontaneous and stimulated emission and absorption in a large variety of molecular rotational-vibration and rotational transitions. In this respect, the MLT has a significant peculiarity related to the fact that the vibrational (and in its upper part also rotational) excitation of the molecules does not obey Boltzmann's law with the local kinetic temperature. As a result, the IR radiation (which is often called "thermal radiation") emitted in these layers does not reflect the thermal state of matter. This situation is referred to as the breakdown of local thermodynamic equilibrium (LTE) for the vibrational or rotational–vibrational degrees of freedom. Detailed treatment of non-LTE plays a crucial role for the estimation of the thermal effects of the IR radiation and for the diagnostics of space-based IR observations.

In the book by López-Puertas and Taylor (2001), the discussion of both topics was presented relying on the current status of research at that time. Since then, many research papers have been published in this field. For example, the recent paper of Funke et al. (2012) contains an updated compilation of the non-LTE models for the most important atmospheric infrared emitters. However, no reviews discussing the current status of methodologies and indicating the directions for further studies have been published for quite a while. This paper is intended (at least partly) to fill this gap. The storyline is built around the studies in which both authors took part and, naturally, other works that to our mind had a significant impact on the field.

The paper is organized as follows. First, we consider the mechanisms of the IR radiation generation in the MLT, discuss the conditions for LTE breakdown using an example of a two-level atom (Sect. 2), and introduce the radiative cooling/heating rate (called "heating rate" throughout this paper, see the definition in Sect. 2.2.4), which is the characteristic essential for understanding the energetic balance in the MLT. This section also contains a description of the research code that is used for all test calculations shown in this work. Section 3 provides the current status of our non-LTE model for carbon dioxide, ozone, and water vapor, the three most important molecules for the IR heating of the MLT. For each of the molecules considered, the calculated heating rates for five typical atmospheric scenarios, from subarctic summer to subarctic winter, are shown. We pay specific attention to the problem of the quenching rate coefficient for energy exchange during CO_2–O collisions and provide details of the most recent study on this topic. We discuss the O_2/O_3 photolysis scheme and the coupling of the photolysis products' energy levels with the system of water vapor vibrational levels. At the end of Sect. 3, we consider an interesting aspect of the

radiative cooling in the MLT that is related to the combined effect of the small-scale temperature and trace gas concentration fluctuations associated with gravity waves, and to the radiative transfer in the 15 μm CO_2 band. Section 4 deals with the optimization of the heating rate calculations necessary for atmospheric modeling. Besides the well-known parameterization methods, we also present an approach that provides accuracy comparable to line-by-line calculations but is faster by a factor of $\sim 10^3$–10^4. Section 5 describes the most common techniques of IR sounding of the MLT and peculiarities of the atmospheric parameter retrievals related to the non-LTE character of radiation emitted from this region. Section 6 presents the conclusions of this work.

2 IR Radiation in the MLT: Generation Mechanisms and Interaction with Matter

2.1 Overview

Optically active molecular gases at any given height in the atmosphere absorb and emit radiation. With respect to the radiative energy transformations, the MLT area can be considered as a mixture of gases exposed to (a) the solar irradiance from the top, (b) the reflected solar radiation from below, (c) the terrestrial IR radiation from below, and (d) the radiation emitted by the molecules in other atmospheric layers (Fig. 1). Solar energy is absorbed primarily by O_2 and O_3 molecules, and their photolysis leads to atmospheric heating both directly (through the formation of translationally hot products) and by creating electronically and vibrationally excited products that later will heat the atmosphere through a set of energy exchange processes. The solar near-infrared radiation in the spectral range with wavelengths $\lambda \leq 5$ μm is also absorbed by a number of molecules to provide the heating of the MLT; among them, the most noteworthy are the CO_2 2.0, 2.7, and 4.3 μm bands. Another source of the MLT heating is the absorption of atmospheric radiation emitted from other atmospheric layers. This heating is accompanied by cooling due to the emission of radiation, mainly in the CO_2 15 μm band, O_3 9.6 μm band, and H_2O rotational and 6.3 μm vibrational bands (e.g., see Brasseur and Solomon 2005). In this work, we will focus mainly on the IR part of the spectra that corresponds to the rotational–vibrational (also called ro-vibrational) transitions of the atmospheric molecules.

If a molecule (or atom) is formed in an excited state due to absorption of a radiation quantum or due to chemical or photochemical processes, then the energy of excitation may be (a) emitted to the atmosphere; (b) transferred to another excited state of the same molecule through an intra-molecular energy exchange induced by collision with another molecule or atom; (c) transferred to other molecules by intermolecular vibrational–vibrational (V–V) or (d) electronic-vibrational (E–V) energy exchange processes; or (e) converted to kinetic energy of atmospheric molecules and atoms via collision (vibrational–translational energy exchange, V–T). A simplified scheme of the interactions between the atmospheric molecules is shown in Fig. 2. In general, each molecule exchanges energy with the heat reservoir through the V–T collisions and interacts with other molecules through a set of V–V and E–V energy exchanges.

To calculate the absorbing and emitting characteristics of the optically active molecules and to estimate the balance between the IR cooling and heating one needs to know the populations of the corresponding ro-vibrational levels. However, as mentioned above, the vibrational levels of the molecules under consideration are not in thermodynamic equilibrium with the surrounding medium in the MLT. The next section provides the background necessary for understanding the non-LTE effects in the atmosphere.
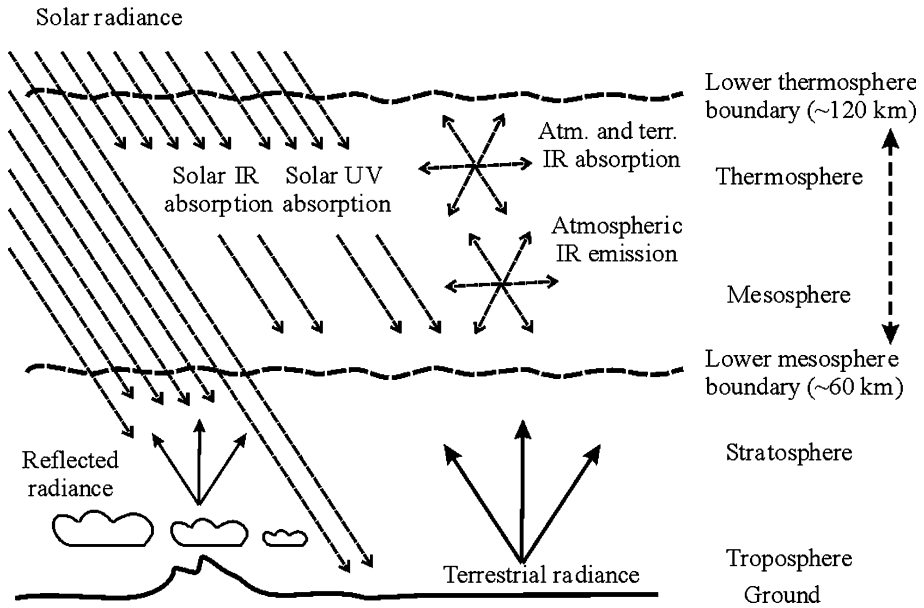
Solar radiance

Fig. 1 Diagram showing radiative processes affecting the MLT region: solar irradiance, reflected and scattered solar radiation (by clouds and from the ground), terrestrial IR radiation, and radiation emitted by other atmospheric layers
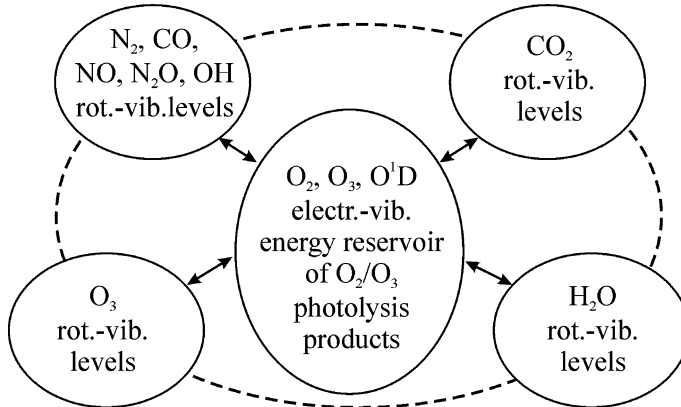

Fig. 2 Diagram illustrating those molecules and atoms whose ro-vibrational and/or electronic levels are involved in the generation of IR emissions in the MLT region. Energy exchange and transformation processes involve absorption of radiation quanta (see Fig. 1), emission to the atmosphere, and collision-induced intra- and inter-molecular V–V, E–V, and V–T energy exchange

2.2 LTE and Non-LTE

2.2.1 The Two-Level Atom

For simplicity, let us first consider a case of a plane-parallel atmosphere that contains just one optically active component: a two-level hypothetical atom. Let us assume that we

consider a steady state of the atomic gas, which means that pressure, temperature, and the degree of excitation (the ratio of the upper-level population to the lower-level population) do not change with time. For this atom, one can write the steady-state equation (SSE), which describes the various processes populating and de-populating each level of the atom at any given altitude, as

$$(R_{21} + C_{21}) \cdot n_2 = (R_{12} + C_{12}) \cdot n_1, \tag{1}$$

where n_1 and n_2 are the populations of the first and second levels, respectively, C_{12} and C_{21} are the coefficients of collisional population and de-population of the second level, and

$$R_{21} = A_{21} + B_{21} \cdot \bar{J}(z), \quad R_{12} = B_{12} \cdot \bar{J}(z) \tag{2}$$

are the radiative terms, where A_{21}, B_{21}, and B_{12} are, respectively, the Einstein coefficients for spontaneous emission, stimulated emission, and absorption, and

$$\bar{J}(z) = \frac{1}{4\pi} \int_\Omega d\Omega \int_{-\infty}^{+\infty} I_{\mu\nu}(z)\varphi(\nu,z)d\nu = \int_{-1}^{1} \int_{-\infty}^{+\infty} I_{\mu\nu}(z)\varphi(\nu,z)d\nu d\mu \tag{3}$$

is the integrated mean intensity of the radiation at the considered altitude. Here, $I_{\mu\nu}(z)$ is the monochromatic radiation intensity, which satisfies the radiative transfer equation (RTE)

$$\mu \frac{dI_{\mu\nu}(z)}{dz} = -\chi_{\mu\nu}(z)I_{\mu\nu}(z) + \eta_{\mu\nu}(z), \tag{4}$$

where $I_{\mu\nu}(z)$ is the monochromatic radiation intensity, $\mu = \cos(\theta)$ is the direction cosine, ν is the frequency of the radiation, $\chi_{\mu\nu}(z)$ and $\eta_{\mu\nu}(z)$ are the total opacity and emissivity, respectively, and $\varphi(\nu, z)$ is the normalized spectral line profile function, which satisfies

$$\int_{-\infty}^{+\infty} \varphi(\nu,z)d\nu = 1. \tag{5}$$

It is important to note that the opacity and emissivity terms in (4) are expressed through the populations of the upper and lower levels as $\chi(z) = \frac{h\nu}{4\pi}(n_1(z)B_{12} - n_2(z)B_{21})$ and $\eta(z) = \frac{h\nu}{4\pi}n_2(z)A_{21}$, respectively. In order to find n_1 and n_2, one must supplement Eq. (1) by the particle conservation law

$$n_1 + n_2 = 1. \tag{6}$$

In general, $\bar{J}(z)$ in the radiative terms R_{21} and R_{12} in (2) in the MLT is the combination of solar radiation, terrestrial radiation, radiation scattered by the clouds, and the atmospheric radiation (see Fig. 1). The system of steady-state Eqs. (1) and (6) can be solved for the populations n_1 and n_2 if all the coefficients A_{21}, B_{21}, B_{12}, C_{21}, C_{12}, and $\bar{J}(z)$ are known. On the other hand, finding $\bar{J}(z)$ requires solving and integrating the radiative transfer Eq. (4), which depends on the populations n_1 and n_2. As a result, one has to search for the joint solution of (1), (6) and (3), (4) (e.g., see Ivanov 1973; Mihalas 1978). There are various approaches to solving this joint system in atmospheric studies: the Curtis method (e.g., see Goody and Yung 1995), Lambda Iterations (e.g., see Wintersteiner et al. 1992), Modified Curtis Method (e.g., see López-Puertas and Taylor 2001; Funke et al. 2012), Accelerated Lambda Iterations (e.g., see Kutepov et al. 1998; Gusev and Kutepov 2003). We will refer to them in Sect. 4.1 with respect to the calculation optimization schemes.

In further consideration of the two-level system, one has to keep in mind that the coefficients C_{12} and C_{21} in (1) are linked by the detailed balance equation

$$C_{21} = C_{12} \frac{g_2}{g_1} e^{-E_{21}/kT}, \tag{7}$$

where k is Boltzmann's constant, E_{21} is the energy difference between the levels, and T is the local temperature. This results from the validity of the Maxwellian distribution for the translational degrees of freedom for molecules and atoms of the atmospheric constituents in the MLT. Correspondingly, if the terms R_{12} and R_{21} in Eq. (1) are negligible in comparison with C_{12} and C_{21} or if $n_1 R_{12} \cong n_2 R_{21}$, then the populations n_1 and n_2 will obey Boltzmann's law. Since the collisional term is proportional to the concentration of the collisional partner, the former situation is typical for the lower atmosphere. The latter situation is possible in the cores of optically thick lines. This is also more typical for the lower atmosphere due to high concentrations of the absorbing gas. We will refer to such conditions as "LTE" (local thermodynamic equilibrium) and we will denote the corresponding level populations as the "LTE populations". If the frequency of collisions is low and $n_1 R_{12} \neq n_2 R_{21}$, then the populations will be sensitive to the radiative field. This situation is called "non-LTE".

2.2.2 The Multi-Level Non-LTE Problem

In reality, the number of levels involved in energy exchange processes in the atmosphere is far greater than two (see Figs. 7, 11, 14 below). In this case, the system of SSE (1), (6) and RTE (4) must be extended to the other levels. Correspondingly, a complete system for N_V vibrational levels will include N_V steady-state equations, one of which must be replaced by a particle conservation equation similar to (6). In the case of a multi-level problem, the collisional terms are divided into two groups: V–T, for which the vibrational state of only one collisional partner changes, and V–V energy exchange processes, for which both of the collisional partners change their vibrational states. In general form, the steady-state equation for a multilevel problem involving chemical production P and losses L can be written as:

$$n_l \left(L_l + \sum_{l \neq l'} (R_{ll'} + C_{ll'}) \right) = \sum_{l \neq l'} n_{l'} (R_{l'l} + C_{l'l}) + P_l \quad (l = 1, 2, \ldots, N_V). \tag{8}$$

Each of the molecules considered is characterized by a set of radiation coefficients, usually obtained from the HITRAN spectroscopic database described in Rothman et al. (2009), and by a set of V–T and V–V rates representing a compilation of the most up-to-date measurements and theoretical calculations.

For the case of a multilevel problem with rotational substructure of vibrational levels, the integrated mean intensity calculation (3) and the radiative transfer Eq. (4) must take into account the ro-vibrational structure of the optical molecular band. In general, for any given pair of ro-vibrational levels (l, l'), where l' is the lower level index and l is the upper level index, the emissivity $\eta_{ll'}(\nu)$ and opacity $\chi_{ll'}(\nu)$ at the frequency ν are given by

$$\eta_{ll'}(\nu) = \frac{h\nu_{ll'}}{4\pi} n_l A_{ll'} \varphi_{ll'}(\nu), \quad \chi_{ll'}(\nu) = \frac{h\nu_{ll'}}{4\pi} (n_{l'} B_{l'l} - n_l B_{ll'}) \varphi_{ll'}(\nu), \tag{9}$$

where $\nu_{ll'}$ is the line center frequency, $A_{ll'}$, $B_{l'l}$, and $B_{ll'}$ are the Einstein coefficients, and $\varphi_{ll'}(\nu)$ is the normalized line profile (see (5)). The total emissivity and opacity expressed in terms of line quantities (9) are

$$\eta(v) = \sum_{l,l'} \eta_{ll'}(v), \quad \chi(v) = \sum_{l,l'} \chi_{ll'}(v). \tag{10}$$

In the traditional approach, the radiative transfer equation is solved for each line separately, and the resulting integrated mean intensities are summed for the molecular band considered. This type of radiative transfer calculations is called LBL (for line-by-line) and is used as a reference because of its high accuracy. The computational cost is high, due to the large number of individual lines involved. In addition, each line in this approach must be well resolved at all altitudes, which means that a large number of spectral points must be considered. In the lower atmosphere, the problem is complicated by line overlapping, which requires a finer spectral grid. Fortunately, in the Earth's atmosphere, line overlapping effects are essentially separated from the non-LTE effects: the lower the pressure, the narrower is the line and the stronger the non-LTE effects. In this work, we will consider only non-overlapping lines, which is a reasonable approximation for the MLT. We will address the computational cost issues and the optimization strategy in the Sect. 4. For more details regarding solving the multi-level non-LTE problem, we refer the reader to the works of Kutepov et al. (1998), López-Puertas and Taylor (2001), and Gusev and Kutepov (2003).

2.2.3 Non-LTE Populations and Vibrational Temperatures

Figure 3 illustrates the typical cases of non-LTE. The levels selected for this demonstration are the upper ones in optically thick (main isotope of CO_2) and optically thin (the fifth in abundance CO_2 isotope) fundamental v_2 (15 μm) and v_3 (4.3 μm), and the vibrational level pumped by direct solar radiance absorption in the 2.0 μm band. In this work, we mark the vibrational levels in accordance with the nomenclature used in the HITRAN spectroscopic database: v_1, v_2, l, v_3, n_F where v_1, v_2, and v_3 denote the number of the corresponding vibrational quanta, the l symbol refers to the angular momentum quantum number, and the n_F symbol denotes the number of the level in a subgroup of levels close in energy and linked by Fermi resonance. The isotopes are marked using the lower digit of the atomic weight: $^{16}O^{12}C^{16}O$ corresponds to 626, $^{16}O^{13}C^{18}O$ is marked as 638, $^1H^{16}O^1H$ becomes 161, and so on.

The vibrational-level populations are traditionally shown as vibrational temperatures that give an insight into the pumping and quenching mechanisms for a given level. The vibrational temperatures T_{vib} describe the excitation degree of the level l against the ground level 0:

$$\frac{n_l}{n_0} = \frac{g_l}{g_0} e^{-(E_l - E_0)/kT_{vib}}, \tag{11}$$

where E_l is the energy of the level l and E_0 is the ground-level energy. If the level is in LTE, then $T_{vib} = T_{kin}$. If $T_{vib} > T_{kin}$ then the net pumping of the level is larger than that under LTE conditions. Similarly, if $T_{vib} < T_{kin}$, the level is populated less efficiently and/or depopulated faster than at LTE.

Let us comment on the behavior of the corresponding T_{vib} in Fig. 3 and explain the physics involved: the temperature difference between the stratopause and the mesopause is not high enough to ensure significant pumping of the 01101 levels by radiation coming from below (see the right-hand panel of Fig. 3); the high optical thickness of the main isotope's v_2 transitions and frequent atmospheric collisions keep the 626(01101) level in LTE up to ~ 80 km altitude; the 638(01101) level is characterized by optically thinner
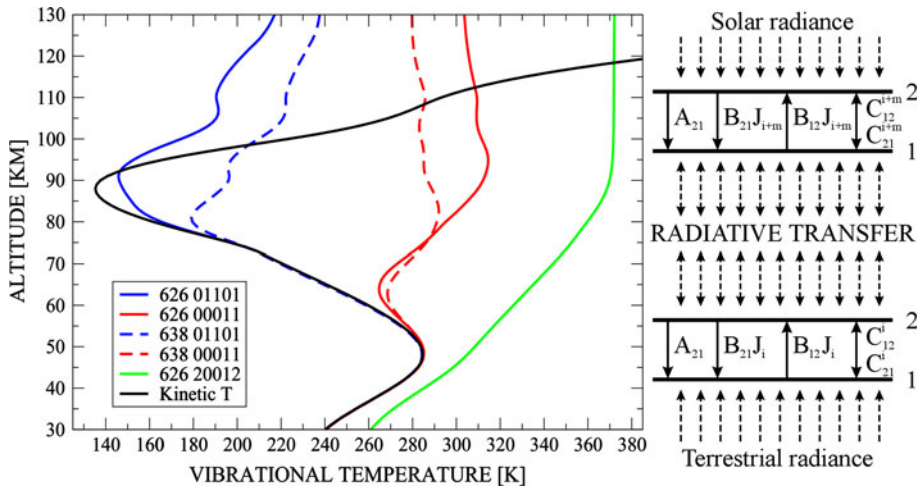
Fig. 3 Explanation of non-LTE effects in the middle and upper atmosphere. *Left*: Vertical temperature distribution in the atmosphere, with a large (>75 K) temperature difference between the stratopause and the mesopause, typical for the high latitude summer atmosphere (latitude = 70°N, solar zenith angle = 46.5°). The non-LTE populations on this plot and below are represented as vibrational temperatures (see text). 626 is the main CO_2 isotope ($^{16}O^{12}C^{16}O$); 638 is the fifth in abundance (4.4×10^{-2}) CO_2 isotope ($^{16}O^{13}C^{18}O$); 01101 and 00011 are first ν_2- and ν_3 vibrational levels, respectively. The 20012 is the solar-pumped vibrational level (see also Fig. 7). *Right*: diagram of energy transformation for the simplified two-level case in a layered plane-parallel atmosphere (i is the index of the layer corresponding to the stratopause, and $i + m$ defines the mesopause level)

"photon escape paths" that leads to LTE breakdown for this level at lower altitudes; the absorption of solar radiation and its further redistribution to the 00011 levels moves them out of LTE at ~55 km altitude. The level 20012 is efficiently pumped by solar radiance absorption in the 2.0-µm band and is in non-LTE even at low altitudes. Following this logic, one may explain the T_{vib} behavior in other cases.

2.2.4 Radiative Cooling and Heating Rates

Radiative cooling and heating are essential energetic characteristics of the atmosphere that show the amount of energy acquired or lost by an atmospheric layer due to the integrated effects of radiative energy absorption and emission. The radiative flux divergence defines the rate at which energy is added to the radiative field per unit volume, that is the rate at which energy is lost by the matter. Following the standard way (see, e.g., Goody et al. 1989), we introduce the radiative heating rate h for this process as the radiative flux divergence taken with the minus sign. In the plane-parallel atmosphere at the altitude z, the flux divergence is obtained by integrating Eq. (4) over frequency and solid angle

$$h(z) = -\frac{1}{4\pi} \int_{\Omega} d\Omega \int_{-\infty}^{+\infty} \mu \frac{dI_{\mu\nu}(z)}{dz} d\nu \tag{12}$$

Since the main effect of interaction between the infrared radiation and the atmosphere is cooling, $h(z)$ is often called "cooling rate", even though it is a heating rate by definition. One has to keep in mind that $h(z)$ may be both positive (heating) and negative (cooling) depending on the dominating term in the right-hand side of Eq. (12). Throughout this paper, we will call

$h(z)$ "heating rate". The units of $h(z)$ in (12) are (W/m^3). To convert the $h(z)$ values to units more commonly used in atmospheric physics (K/day), one has to apply the formula

$$h(z)(\text{K/day}) = h(z)(\text{W/m}^3)\frac{24 \cdot 60 \cdot 60}{C_p(z)\rho(z)}, \tag{13}$$

where $C_p(z)$ is the heat capacity at constant pressure in (J/kg/K), and $\rho(z)$ is the density in (kg/m^3). We note here that heating rate in (K/day) should not be treated as daily averages; "day" is used as time unit while $h(z)$ can (and does) vary during the day. We suppose that the integral over frequency in (12) covers the entire IR range and will show the altitude distributions for the net heating rate $h(z)$. The sign of $h(z)$ tells whether the atmosphere is cooled or heated at the given altitude z, and its magnitude provides an estimate of the importance of a given molecule for the energetic balance of the region. The heating rate distributions will be accompanied by plots showing the $n_l(z)$ distributions for the most important vibrational levels. In Sect. 3, we will consider the non-LTE radiative heating rates for the main contributors to the MLT radiative energy budget: CO_2, O_3, H_2O, and the kinetics of the O_2/O_3 photolysis products.

2.3 ALI-ARMS Research Code

All calculations presented in this work were performed with the help of the ALI-ARMS (for Accelerated Lambda Iterations for Atmospheric Radiation and Molecular Spectra) non-LTE code package described in detail in Kutepov et al. (1998), Gusev and Kutepov (2003), and Gusev (2003). Compared to the other non-LTE codes applied in the studies of the Earth's and planetary atmospheres, the ALI-ARMS code solves the multi-level problem (8) by means of the accelerated lambda iteration (ALI) technique developed in stellar astrophysics (e.g., see Rybicki and Hummer 1991, 1992; Pauldrach et al. 1994, 2001; Pauldrach 2003; Hubeny and Lanz 2003; Hubeny et al. 2003) for calculating non-LTE populations of atomic and ionic levels (see also Sect. 4.1 of this paper).

The code in its current version can treat an arbitrary number of molecules of arbitrary structures in a given planetary atmosphere provided by the prescribed format inputs of (a) planetary atmosphere profile that consists of pressure, temperature, volume mixing ratios (VMRs) of molecules at all altitudes, (b) solar spectra, (c) vibrational and ro-vibrational energies, (d) spectroscopic information (the Einstein coefficients for ro-vibrational or rotational transitions, line half-widths), and (e) collisional rate coefficients for specified sets of E–V, V–T, and V–V transitions. The code produces populations of ro-vibrational levels and radiative flux divergences (radiative cooling and heating) in the lines and bands involved.

The current inputs of V–T and V–V rates are described in Shved et al. (1998), Manuilova et al. (1998) and summarized in the Ph.D. thesis by Gusev (2003). These inputs include the interactions between the following molecules: N_2, O_2, CO_2, O_3, H_2O, CO, OH, and NO (Fig. 2). The reference model (Fig. 4) includes 350 vibrational levels and 200,000 ro-vibrational lines of the CO_2 molecule and its isotopes (Sect. 3.1), 23 vibrational levels and 150,000 ro-vibrational lines of ozone (Sect. 3.2), 14 vibrational levels and 20,000 lines of the H_2O molecule (Sect. 3.4), and 7 vibrational levels of N_2 molecule. The model also incorporates the kinetic model of O_2/O_3 photolysis products (Sect. 3.3) developed by Yankovsky and Manuilova (2006) and interactions of the photolysis products with vibrational levels of H_2O, N_2, and CO_2 molecules.

The ALI-ARMS code has been successfully applied to the interpretation of the 4.3- and 9.6-μm spectral Earth's limb radiation measured by the Cryogenic Infrared Spectrometers and Telescopes for the Atmosphere (CRISTA) instrument (see Offermann et al. 1999;
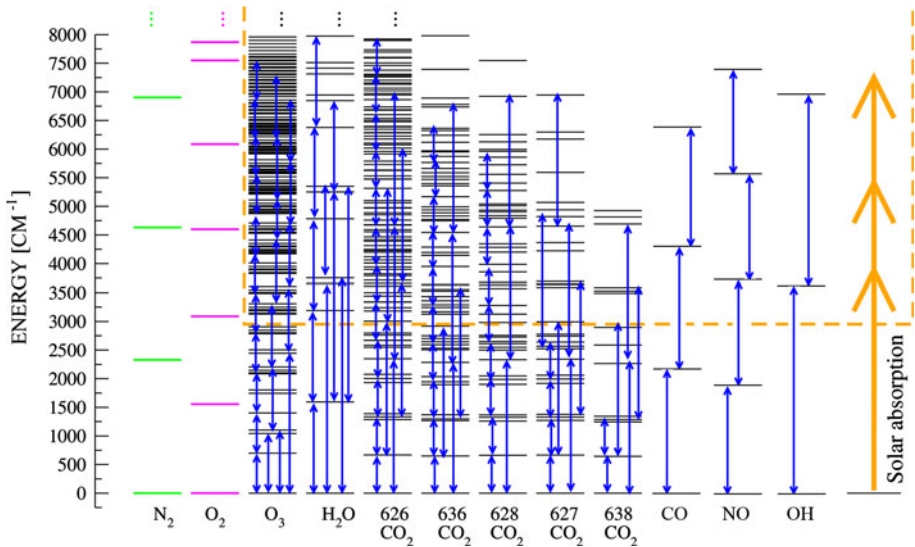
Fig. 4 Vibrational energy levels diagram for molecules considered in this study, which are included in the current ALI-ARMS reference model. Levels for CH_4 and N_2O molecules, which are also part of the model, are not shown. *Thin black lines*: vibrational levels. *Blue lines* with *arrows*: major fundamental and hot optical transitions. *Dashed orange line*: the vibrational level manifold pumped by the absorption of near-IR solar radiation (*thick orange arrow*). The vibrational levels are linked by a variety of V–T and V–V energy exchanges (not shown here, see Sect. 3 for more details)

Grossmann et al. 2002) in the studies by Kaufmann et al. (2002, 2003) who retrieved the first global CO_2 and O_3 density distributions in the Earth's MLT. Later Gusev et al. (2006) applied the ALI-ARMS model to the analysis of the CRISTA 15 μm spectral radiation data and performed temperature retrievals in the MLT. The ALI-ARMS code was used for the analysis (see Maguire et al. 2002) of the seasonal, altitude, and latitude variations of the 10 μm CO_2 limb emissions measured by the Thermal Emission Spectrometer onboard the Mars Global Surveyor (TES/MGS), as well as to study the infrared radiative heating of the middle and upper atmospheres of Mars (see Hartogh et al. 2005) and Earth (e.g., see Kutepov et al. 2007).

The ALI-ARMS code was also used (see Kutepov et al. 2006, Feofilov et al. 2009, Rezac 2011) for the validation of the operational retrieval algorithms applied to processing broadband 15 and 4.7 μm CO_2 and 6.3 μm H_2O Earth's limb emissions measured by the SABER (Sounding of the Atmosphere using Broadband Emission Radiometry) instrument (see Russell et al. 1999) on board the NASA TIMED (Thermosphere Ionosphere Mesosphere Energetics and Dynamics) satellite (see Yee et al. 1999). It was also used for the analysis of the MGS-TES 15 μm limb observations to extend temperature retrievals in Martian atmosphere up to ∼90 km altitude (see Feofilov et al. 2012b) and for developing the two-channel algorithm for simultaneous retrieval of pressures/temperatures and CO_2 VMRs in the MLT from the SABER limb 15 and 4.3 μm radiation (see Rezac 2011).

2.4 Test Atmospheres Used in Study

To demonstrate the variability of the infrared energy budget components in the MLT, we used five typical atmospheric scenarios. The time of the year for all of the test profiles was

Table 1 Atmospheric scenarios used in this study

Name Day/night	SAW Twilight/night	MLW Day/night	TROP Day/night	MLS Day/night	SAS Days
Noon θ_z	93.5°	63.5°	23.5°	16.5°	46.5°
Latitude	70°S	40°S	0°	40°N	70°N
SABER day					
DOY	193	194	193	193	193
Latitude	69.4°S	39.8°S	0.1°N	38.0°N	68.4°N
Longitude	180.6°	158.2°	210.2°	14.7°	95.8°
θ_z	92.24°	63.1°	28.3°	25.3°	49.7°
SABER night					
DOY	194	194	192	192	
Latitude	68.14°S	40.0°S	0.1°S	38.1°N	–
Longitude	208.1°	273.5°	318.6°	175.9°	
θ_z	131.0°	154.8°	154.5°	119.4°	

set to the summer solstice in the Northern hemisphere. The time of the day was set to local noon. Pressure/temperature profiles, O_2, and N_2 VMR profiles were obtained from the MSIS-E-90 database (http://omniweb.gsfc.nasa.gov/vitmo/msis_vitmo.html). The CO_2 VMRs were taken from WACCM model outputs (http://waccm.acd.ucar.edu/). Because the O_3, $O^3(P)$, and $O^1(D)$ values are highly variable and are interdependent, we used the correspondent VMRs obtained from the SABER V1.07 "instantaneous" retrievals (http://saber.gats-inc.com/). The H_2O VMRs are July averages retrieved from all ACE-FTS measurements (see Bernath et al. 2005). In this work, we will use abbreviated names for these five atmospheric scenarios: SAW for subarctic winter, MLW for midlatitude winter, TROP for the tropical atmosphere, MLS for midlatitude summer, and SAS for subarctic summer. The latitudes and solar zenith angles for local noon, θ_z, and the SABER 2010 orbits and record numbers are listed in Table 1.

Figure 5 shows the temperature profiles used in the study. These profiles cover most of the situations that are observed in the atmosphere, unperturbed by gravity waves (GW, see Sect. 3.5).

Even though the area of our primary interest is the MLT, pressure/temperature and trace gases VMR distributions in the lower atmosphere are also necessary due to non-local effects and pumping the molecular levels in the MLT by radiation coming from below. Some features of the selected profiles are worth noting: the stratopause temperature varies from 255 K (MLW) to 281 K (SAS), the mesopause temperature changes from 140 K (SAS) to 200 K (SAW) (see the discussion in Smith 2012), and the θ_z changes from 16.5° (MLS) to 93.5° (SAW). One has to keep in mind that even though $\theta_z = 93.5° > 90.0°$ means night on the ground, the SAW atmosphere is in shadow only up to ~ 12 km while, above this point, the atmosphere is still illuminated so this specific case is called "twilight" in Table 1. The maximum of the solar pumping and O_2/O_3 photodissociation in this case moves up, contrary to the low θ_z case for MLS atmospheric scenario. Figure 6 shows the vertical distributions of the CO_2, O_3, H_2O, $O(^3P)$, and $O(^1D)$ VMRs. It is essential to include both daytime and nighttime ozone profiles because of the second ozone maximum at ~ 90 km during the nighttime.
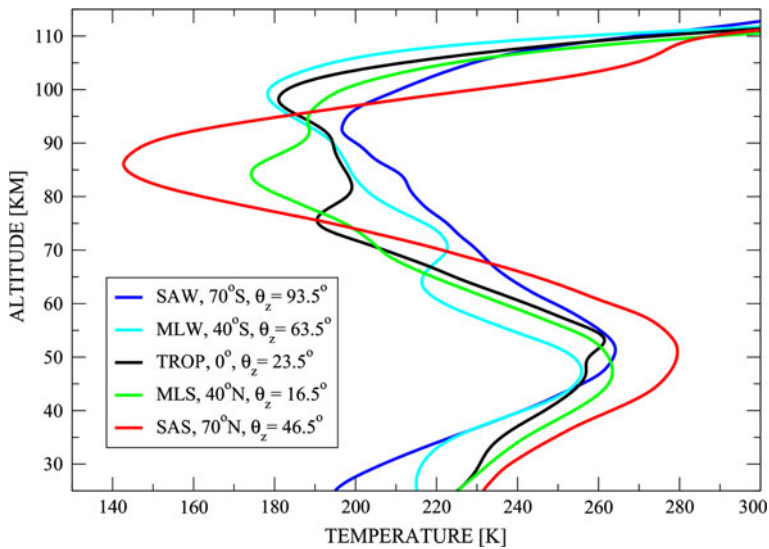
Fig. 5 Atmospheric temperature profiles used for heating rate calculations, infrared radiation profiles estimates, and testing the optimized heating rate calculation schemes: SAW denotes subarctic winter, 70°S, solar zenith angle $\theta_z = 93.5°$; MLW denotes midlatitude winter, 40°S, $\theta_z = 63.5°$; TROP stands for tropical profile, 0°, $\theta_z = 23.5°$; MLS denotes midlatitude summer, 40°N, $\theta_z = 16.5°$; SAS stands for subarctic summer, 70°N, $\theta_z = 46.5°$

3 Radiative Cooling and Heating in the MLT

The main objective of this section is to provide an overview of CO_2, O_3, O_2, and H_2O contributions to the energy budget of the MLT, and to discuss the energy transformation mechanism in which these molecules are involved. This requires considering the non-LTE models for the CO_2, O_3, and H_2O molecules as well as the model of O_2/O_3 photolysis products kinetics.

3.1 Carbon Dioxide

Carbon dioxide is an optically active linear triatomic molecule. It has the three vibrational modes: linear symmetric and asymmetric stretch vibrations referred to as ν_1 and ν_3, respectively, and bending mode (ν_2). The vibrational quanta energies are 1,388, 667, and 2,349 cm^{-1} for ν_1, ν_2, and ν_3 modes, respectively. The CO_2 vibrational levels diagram with the main optical transitions and processes of V–V exchange is shown in Fig. 7. The levels on this diagram are marked in accordance with the HITRAN notation described in Sect. 2.2.3. A CO_2 molecule takes part in the following processes essential for the MLT energetics: solar radiation absorption in 1–4.3-μm bands, CO_2 atmospheric radiation absorption and emission, and redistribution of the excitation among various vibrational levels in a series of V–V, V–T, and emission processes.

Let us consider in detail the 15-μm infrared emission ($I_{15\ \mu m}$) formation. This emission is the dominant cooling mechanism in the Earth's MLT (e.g., see Gordiets 1976; Dickinson 1984; Goody and Yung 1995; Sharma and Wintersteiner 1990). On Earth, the magnitude of the MLT cooling affects both the mesopause temperature and height; the stronger the cooling, the colder and higher is the mesopause (see Bougher et al. 1994). The main
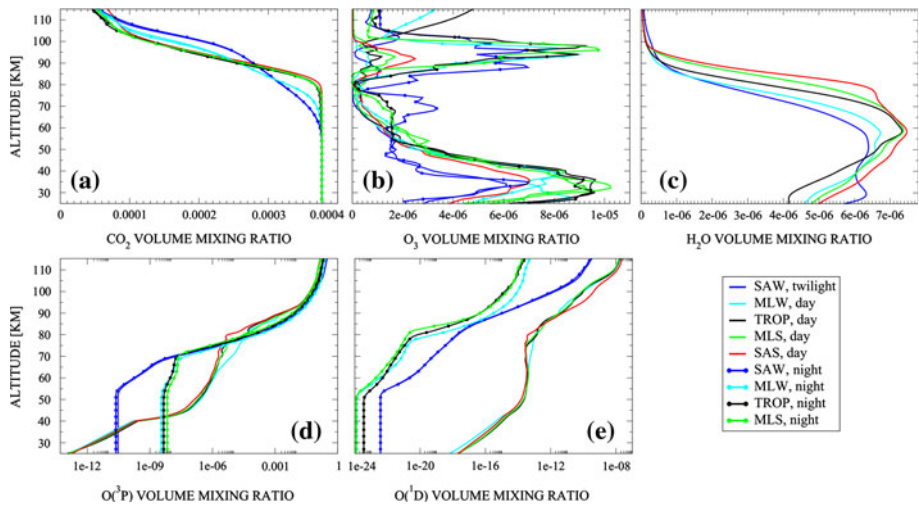
Fig. 6 Volume mixing ratios of CO_2, O_3, H_2O, $O(^3P)$ and $O(^1D)$ used in heating rate calculations, infrared radiation profile estimates, and testing the optimized heating rate calculation schemes: (**a**) SAW, (**b**) MLW, (**c**) TROP, (**d**) MLS, (**e**) SAS

processes linking the 15-μm CO_2 atmospheric radiation to the heat reservoir (translational degrees of freedom of atmospheric constituents) are the inelastic collisions of CO_2 molecules with $O(^3P)$ atoms: first, $O(^3P)$ atom excites the CO_2 bending vibrational mode during the collision:

$$CO_2(v_2) + O(^3P) \rightarrow CO_2(v_2 + 1) + O(^3P), \tag{14}$$
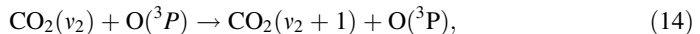
after which the excitation may be (a) quenched by another collision with some molecule or atom, (b) transferred to excited vibrational state of another molecule through the V–V exchange, or (c) transformed to a quantum of radiation: $CO_2(v_2 + 1) \rightarrow CO_2(v_2) + h\nu$ (667 cm^{-1}). To be consistent with the generally accepted way of describing this process, we will refer to the rate coefficient of the reaction inverse to (14) and will call it the "CO_2–O quenching rate coefficient" or k_{VT}, where VT stands for vibrational–translational type of interaction. Generally, it is assumed that the velocity distribution of $O(^3P)$ atom is Maxwellian and that the fine structure of atomic oxygen does not affect the process (14) and its inverse. We will discuss the validity of these assumptions later in Sect. 3.1.2.

Both the radiative heating and $I_{15 \ \mu m}$ strongly depend on k_{VT}, see Sect. 3.1.2. It is, therefore, self-evident that both the calculation of radiative heating rates in CO_2 and the interpretation of measured $I_{15 \ \mu m}$ radiation require the best possible knowledge of k_{VT}. However, despite the importance of k_{VT} for the atmospheric applications, the values, obtained in a laboratory and retrieved by fitting the space observations, vary by a factor of 3–4 (see Table 2). We draw attention to the uncertainty of the k_{VT} quenching rate since its effects on the cooling are comparable to the contributions of all the other radiative heating mechanisms as illustrated below.

3.1.1 Sensitivity of MLT Cooling to the k_{VT} Quenching Rate

To demonstrate the sensitivity of calculated $CO_2(v_2)$ levels populations and, therefore, that of $I_{15 \ \mu m}$ and the CO_2 heating rate, we performed the following sensitivity study. For each

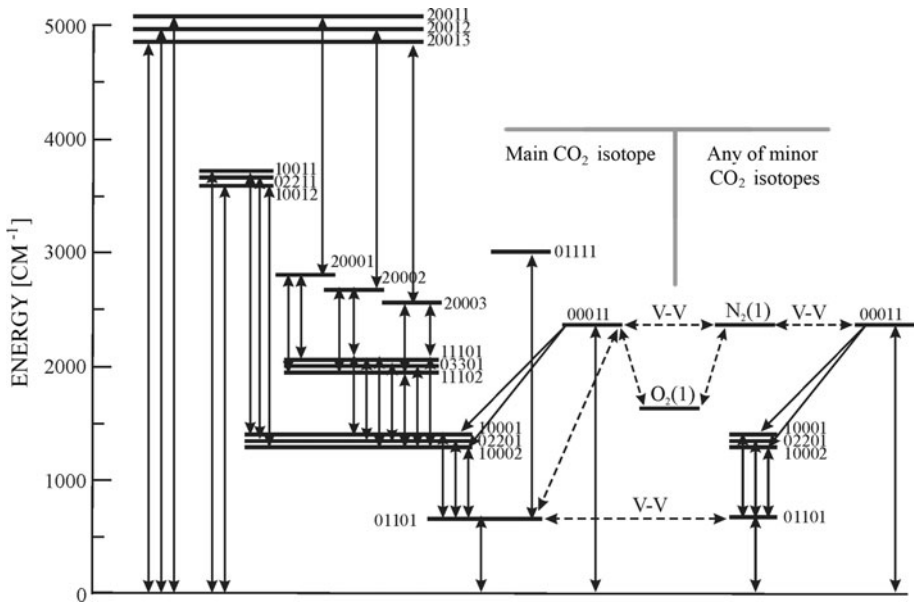**Fig. 7** CO_2 vibrational levels diagram. The levels are marked in accordance with the HITRAN notation (Sect. 2.2.3). *Solid lines* with *arrows* show optical transitions, *dashed lines* with *arrows* refer to the intermolecular V–V energy exchange processes, V–T transitions are not shown for the sake of readability. The main isotope levels are shown up to the 5,000 cm^{-1} energy level, the minor isotopes are shown only up to 00011 level for simplicity

of five test atmospheres described in Sect. 2.4, we solved the non-LTE problem twice. In the first run, k_{VT} was set to 1.5×10^{-12} cm^3 s^{-1}, the value that is close to laboratory measurements (see Table 2). For the second run, k_{VT} was set to 6.0×10^{-12} cm^3 s^{-1}, which is typically retrieved from atmospheric measurements. A standard $(T/300)^{1/2}$ scaling factor for the temperature dependence of the k_{VT} was used. In these calculations, we applied the CO_2 non-LTE model that included 60 vibrational levels of 5 CO_2 isotopes as well as the first excited vibrational levels of N_2 and O_2. Compared to our extended reference model of CO_2 described in Sect. 2.3, this reduced model is accurate within 0.05 K for the $CO_2(\nu_2 = 1,2)$ vibrational temperatures and 0.03 K/day for net CO_2 radiative cooling and heating rates. The results are presented in Figs. 8 and 9. Figure 8 shows the response of two $CO_2(\nu_2)$ levels of the main isotope to k_{VT} changes. As one can see, for all five of the test atmospheres, the non-LTE effects become noticeable above ~ 80 km altitude.

The altitudinal behavior of the $CO_2(\nu_2)$ level populations has the same pattern for all five model atmospheres: the populations move farther from LTE with increasing height. The deviation from LTE depends on the atmospheric scenario: SAW, MLW, and TROP atmospheres demonstrate weaker non-LTE effects compared to MLS and, especially, SAS atmospheres. This is explained by larger temperature differences between the stratopause temperatures and the mesospheric temperatures in the latter two models: the warmer stratopause region produces stronger upwelling $I_{15 \ \mu m}$ radiation flux, which pumps $CO_2(\nu_2)$ levels in the MLT. The response of the $CO_2(\nu_2)$ levels population to the V–T rate coefficient is straightforward (compare blue curves in Fig. 8a–d to the red ones): higher k_{VT} leads to more efficient thermalizing of the $CO_2(\nu_2)$ levels and moves their vibrational

Table 2 Historic review of the k_{VT} quenching rate coefficient laboratory measurements and atmospheric retrievals at $T = 300$ K

k_{VT} (cm^3 s^{-1})	Reference	Comments
3–30×10^{-14}	Crutzen (1970)	First guess
2.4×10^{-14}	Taylor (1974), Center (1973)	Laboratory measurements
5.0×10^{-13}	Sharma and Nadile (1981)	Atmospheric retrieval
1.0×10^{-12}	Gordiets et al. (1982)	Numerical experiment
2.0×10^{-13}	Kumer and James (1983)	Atmospheric retrieval
2.0×10^{-13}	Dickinson (1984); Allen et al. (1980)	Laboratory measurements
5.2×10^{-12}	Stair et al. (1985)	Atmospheric retrieval
3.5×10^{-12}	Sharma (1987)	Atmospheric retrieval
3–9×10^{-12}	Sharma and Wintersteiner (1990)	Atmospheric retrieval
1.5×10^{-12}	Shved et al. (1991)	Laboratory measurements
1.3×10^{-12}	Pollock et al. (1993)	Laboratory measurements
3–6×10^{-12}	López-Puertas et al. (1992)	Atmospheric retrieval
5.0×10^{-12}	Ratkowski et al. (1994)	Atmospheric retrieval
5.0×10^{-13}	Lilenfeld (1994)	Laboratory measurements
1.5×10^{-12}	Vollmann and Grossmann (1997)	Atmospheric retrieval
1.4×10^{-12}	Khvorostovskaya et al. (2002)	Laboratory measurements
1.8×10^{-12}	Castle et al. (2006)	Laboratory measurements
6.0×10^{-12}	Gusev et al. (2006)	Atmospheric retrieval
1.5×10^{-12}	Huestis et al. (2008)	Recommended value
1.3–2.7×10^{-12}	Castle et al. (2012)	Laboratory measurements
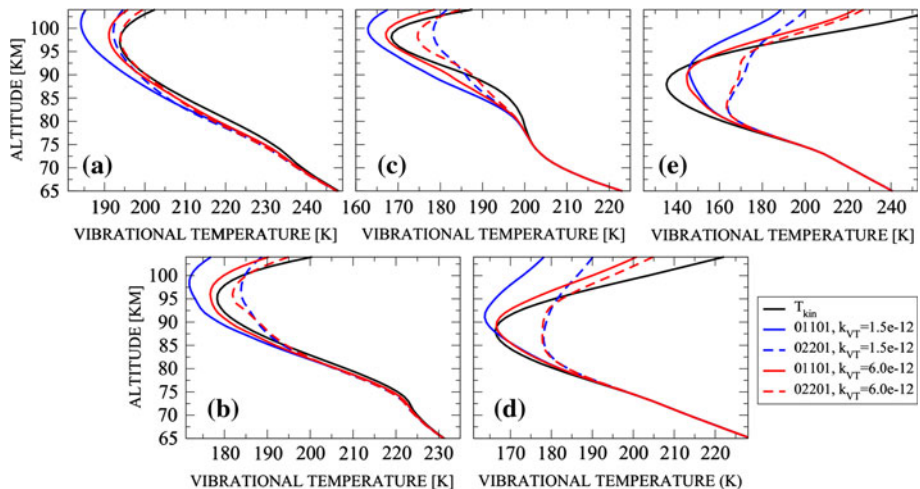
Fig. 8 Sensitivity of 01101 and 02201 vibrational levels population to k_{VT} for the five test daytime atmospheres: (**a**) SAW (twilight case), (**b**) MLW, (**c**) TROP, (**d**) MLS, **e** SAS. *Solid black lines*: kinetic temperature; *red lines*: calculations with $k_{VT} = 6.0 \times 10^{-12}$ cm^3 s^{-1}; *blue lines*: calculations with $k_{VT} = 1.5 \times 10^{-12}$ cm^3 s^{-1}; *solid red* and *blue lines*: populations of 01101 level, *dashed red* and *blue lines*: populations of 02201 level
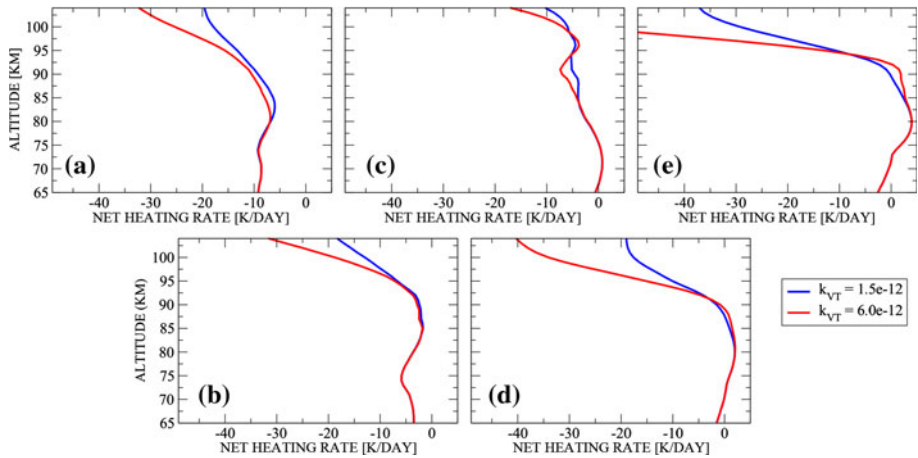
Fig. 9 Sensitivity of net CO_2 heating rate to the value of the $k_{VT}\{CO_2$–O$\}$ quenching rate for the five test daytime atmospheres: (**a**) SAW (twilight case), (**b**) MLW, (**c**) TROP, (**d**) MLS, (**e**) SAS. *Blue lines*: calculations with $k_{VT} = 1.5 \times 10^{-12}$ cm^3 s^{-1}; *red lines*: calculations with $k_{VT} = 6.0 \times 10^{-12}$ cm^3 s^{-1}

temperatures closer to the kinetic temperature profiles. The net heating rates for the five test atmospheres and their sensitivity to k_{VT} are presented in Fig. 9a–d. As one can see, the absolute values of the net heating in the MLT are sensitive both to k_{VT} and to the type of atmosphere. The latter is explained not only by temperature profile differences but also by variability of atomic oxygen VMR profiles. The k_{VT} value and the atomic oxygen concentration are both equally important for the estimation of the MLT CO_2 radiative cooling and $I_{15 \ \mu m}$ since the $CO_2(\nu_2)$ quenching term contains their product (see Eq. (15) below). The strongest MLT cooling in Fig. 9 corresponds to high altitudes, high k_{VT} rate, and polar latitudes in the summer hemisphere. The sensitivity to k_{VT} grows with increasing altitude because the atomic oxygen concentration increases with height. Since the process (14) plays an important role in the MLT cooling, the best possible knowledge of k_{VT} is required for adequate infrared cooling calculations. In the next section, we demonstrate an example of estimating k_{VT} from atmospheric measurements and discuss the result with respect to the MLT energetics.

3.1.2 Estimating k_{VT} Quenching Rate from Atmospheric Observations

The laboratory measurements of rate coefficients for various energy exchange processes by inelastic collisions of molecules and atoms suffer from difficulties with reproducing conditions close to those in the MLT in which molecules and atoms of various compounds interact. This is particularly true for laboratory studies of reactions involving oxygen atoms due to their extremely high chemical activity. On the other hand, the large variety of space and ground-based observations of the MLT available today provides an opportunity to utilize the MLT as "a natural laboratory" for retrieving these critical parameters. Below we discuss a recent example of the k_{VT} retrieval which utilizes the synergy of coincidental satellite and lidar observations of the MLT. The advantage of utilizing the lidar (e.g., see Weitkamp 2005) for such experiments is that the lidar temperature retrievals $T(z)$ do not depend on the non-LTE model parameters and, therefore, can be used as references. The detailed description of the approach is given elsewhere (see Feofilov et al. 2012a). The
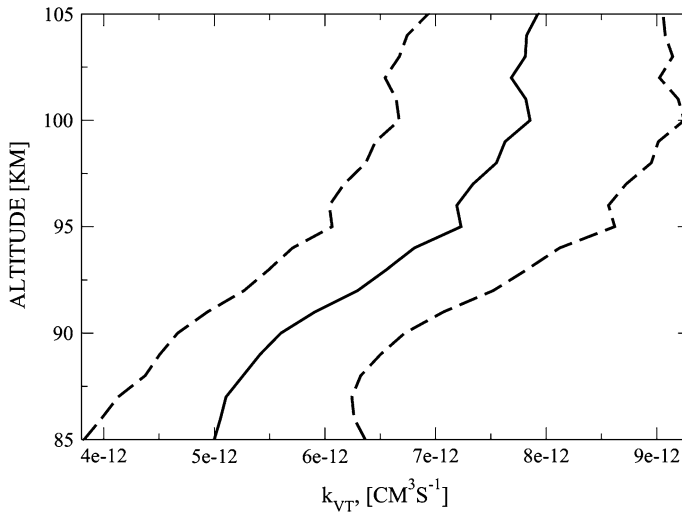
Fig. 10 *Solid line*: $k_{VT}(z)$ vertical distribution retrieved from minimizing the differences between the calculated and measured $I_{15 \mu m}(z)$ radiation profiles (from Feofilov et al. 2012a). *Dashed lines:* uncertainties

comparison of the SABER temperature retrievals with lidar measurements has already been performed by Remsberg et al. (2008), and the quenching rate coefficient used in that study was estimated to be equal to $(6.0 \pm 3.0) \times 10^{-12}$ cm^3 s^{-1}. Applying stringent overlapping criteria and treating the individual altitude layers of the overlapping region separately, one can increase the accuracy and get into more detail of the MLT physics.

The general idea of the k_{VT} retrieval is in minimizing the difference between the measured and simulated 15-μm radiation by varying the product of k_{VT} and O(^{3}P) VMR. For the study described, the measured radiation was provided by the SABER instrument that also provides O(^{3}P)(z) (see Smith et al. 2010) and CO$_2(z)$(see Rezac 2011) VMRs. This dataset was supplemented with $T(z)$ in 80–110 km altitude range measured by the Fort Collins lidar (see She et al. 2003). For these temperature profiles, the $I_{15 \mu m}$ limb radiation was simulated at each tangent height in the 85–105 km altitude interval, and the "χ^2" deviations (see Chap. 15 in Press et al. 2002) for the measured and simulated radiation were built for the k_{VT} varying from 1.0×10^{-12} cm^3 s^{-1} to 1.0×10^{-11} cm^3 s^{-1} with a 5.0×10^{-13} cm^3 s^{-1} step. Figure 10 shows the averaged $k_{VT}(z)$ "profile" obtained by Feofilov et al. (2012a) that minimizes the radiation deviation.

Overall, the k_{VT} values shown in Fig. 10 fit the atmospheric retrievals well: the averaged $k_{VT} = (6.5 \pm 1.5) \times 10^{-12}$ cm^3 s^{-1}. However, Fig. 10 also shows the altitudinal variability of k_{VT} that goes beyond its uncertainties in the 85–105 km altitude range. Obviously, this variability does not imply that the rate coefficient depends on altitude. Possible reasons for the k_{VT} "variability" are discussed in Feofilov et al. (2012a) and include collisions with thermal and non-thermal hydrogen, electronically excited O(^{1}S), charged components, multi-quantum excitation of CO$_2$ by thermal oxygen (Ogibalov 2000), and temperature dependence of the k_{VT}. The authors suggest that the observed phenomenon may be explained by the simplicity of the currently utilized CO$_2$ non-LTE model with respect to CO$_2$–O collisions. That might also be a clue to the "atmospheric/ laboratory" difference of the k_{VT} values. The standard pumping term in the non-LTE

model, which describes the total production of CO_2 (v_2) in the state with the number of bending mode quanta v_2 due to collisions with the $O(^3P)$ atoms, has the form of

$$Y_{v_2} = n_{O(^3P)} \{ n_{v_2-1} k_{v_2-1,v_2} - n_{v_2} k_{v_2,v_2-1} \}, \tag{15}$$

where $n_{O(^3P)}$ is the $O(^3P)$ density, n_{v_2-1} and n_{v_2} are the vibrational states populations, and k_{v_2-1,v_2} and k_{v_2,v_2-1} are rate coefficients for one-quantum excitation and de-excitation, respectively.

In the current non-LTE models, including the one applied in this study, it is usually assumed that $k_{v_2-1,v_2} = k_{0,1}$ and $k_{v_2,v_2-1} = k_{1,0} = k_{VT}$. It follows from Huestis et al. (2008) that if the velocity distribution of $O(^3P)$ atoms is Maxwellian and their fine structure is thermalized, then the laboratory measured $k_{0,1}$ and $k_{1,0}$ are linked by the detailed balance relation:

$$k_{0,1} = k_{1,0} \frac{g_1}{g_0} e^{-(E_1-E_0)/kT}, \tag{16}$$

where E_1 is the vibrational energy of the first v_2 vibrational level and E_0 is the energy of ground vibrational level. Sharma et al. (1994) showed that both aforementioned conditions are valid for $O(^3P)$ atoms in the Earth's atmosphere up to at least 400 km, which seems to justify usage of (16) in the non-LTE models. However, as Balakrishnan et al. (1998) and Kharchenko et al. (2005) show, the non-thermal $O(^3P)$ and $O(^1D)$ atoms are produced by O_2 and O_3 photolysis and O_2^+ dissociative recombination reactions in the MLT. These "hot" atoms may serve as an additional source of $CO_2(v_2)$ level excitation. Therefore, the expression (15) may need to be replaced by an expression like

$$Y_{v_2} = n_{O(^3P)} \left\{ (1-\alpha)\{ n_{v_2-1} k_{v_2-1,v_2} - n_{v_2} k_{v_2,v_2-1} \} + \alpha \left\{ \sum_v n_{v_2-v} k_{v_2-v,v_2}^{\text{hot}} - n_{v_2} \sum_v k_{v_2,v_2-v}^{\text{hot}} \right\} \right\}, \tag{17}$$
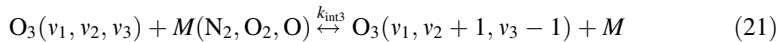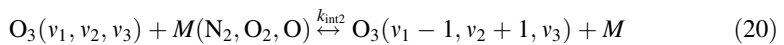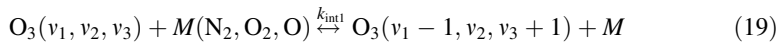
where α is the altitude dependent fraction of total $O(^3P)$ density that corresponds to hot atoms and $k_{v_2-v,v_2}^{\text{hot}}$ and $k_{v_2,v_2-v}^{\text{hot}}$ are the rate coefficients for excitation and de-excitation of CO_2 molecules, respectively, due to collisions with hot atoms, assuming also multi-quantum processes. These rate coefficients are not related by the detailed balance since hot $O(^3P)$ atoms are not thermalized. Comparing (15), which is applied in the model used in the present study, with (17), one can see that the rate coefficient values retrieved in this work and also in earlier atmospheric studies are some sort of effective rate coefficients that include the contribution of hot $O(^3P)$ atoms, which may be expressed as

$$k_{VT}^{\text{retr}}(z) = k_{v_2,v_2-1}^{\text{retr}}(z) = (1-\alpha(z)) \cdot k_{v_2-1,v_2} + \alpha(z) \cdot \sum_v n_{v_2} k_{v_2-v,v_2}^{\text{hot}}. \tag{18}$$
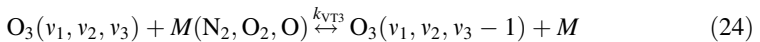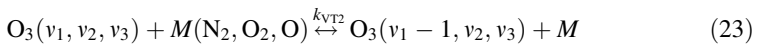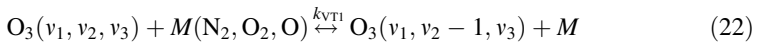
These "hot" atoms may serve as an additional source of $CO_2(v_2)$ level excitation that would explain the difference between the laboratory measurements and atmospheric retrievals of k_{VT}. The increasing hot $O(^3P)$ atoms density with increasing altitude in the MLT may also explain the altitude dependence of the retrieved "efficient" k_{VT}. We stress here that these important questions remain open and require further studies, both theoretical and experimental. The negative temperature dependence of k_{VT} that was found recently (see Castle et al. 2012) makes this problem more complicated since the altitude gradient of the k_{VT} parameter would be even higher if this "new" temperature dependence was to be used in the k_{VT} retrieval.
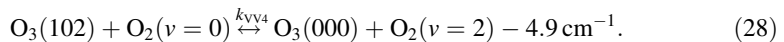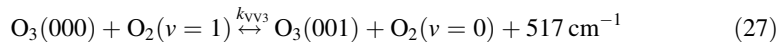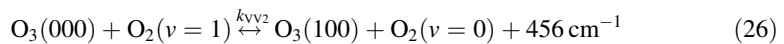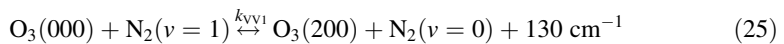
3.2 Ozone

The ozone molecule in its ground electronic state is a bent three-atomic molecule that has three vibrational modes: symmetric and asymmetric stretching modes (v_1 and v_3, respectively), and a bending mode (v_2). The v_1 and v_3 vibrations are close in energy (1,103 and 1,043 cm^{-1}, respectively) and are coupled through a near-resonant V–V exchange. The radiative transitions corresponding to v_1 and v_3 quanta change are responsible for infrared cooling in the 9.6 μm O_3 band. The v_2 band transitions (705 cm^{-1}) are weak and overlap with 15 μm CO_2 emissions. The transitions from the combination level (101) to the ground and hot transitions of the type $(v_1, v_2, v_3) \rightarrow (v_1 - 1, v_2, v_3 - 1)$ give rise to a strong 4.8-μm band. In modern non-LTE models of O_3 (e.g., see López-Puertas and Taylor 2001; Kaufmann et al. 2006; Fernandez et al. 2009, 2010), the total number of vibrational levels considered is more than a hundred, up to the dissociation limit ($\sim 8,500$ cm^{-1}), and includes many combination vibrational states. A simplified diagram of the first 22 vibrational levels of ozone and interactions between them is shown in Fig. 11. The non-LTE model for O_3 molecule involves intra-molecular energy exchange processes:

$$O_3(v_1, v_2, v_3) + M(N_2, O_2, O) \overset{k_{int1}}{\leftrightarrow} O_3(v_1 - 1, v_2, v_3 + 1) + M \tag{19}$$

$$O_3(v_1, v_2, v_3) + M(N_2, O_2, O) \overset{k_{int2}}{\leftrightarrow} O_3(v_1 - 1, v_2 + 1, v_3) + M \tag{20}$$

$$O_3(v_1, v_2, v_3) + M(N_2, O_2, O) \overset{k_{int3}}{\leftrightarrow} O_3(v_1, v_2 + 1, v_3 - 1) + M \tag{21}$$

as well as V–T processes:

$$O_3(v_1, v_2, v_3) + M(N_2, O_2, O) \overset{k_{VT1}}{\leftrightarrow} O_3(v_1, v_2 - 1, v_3) + M \tag{22}$$

$$O_3(v_1, v_2, v_3) + M(N_2, O_2, O) \overset{k_{VT2}}{\leftrightarrow} O_3(v_1 - 1, v_2, v_3) + M \tag{23}$$

$$O_3(v_1, v_2, v_3) + M(N_2, O_2, O) \overset{k_{VT3}}{\leftrightarrow} O_3(v_1, v_2, v_3 - 1) + M \tag{24}$$

and intermolecular V–V processes:

$$O_3(000) + N_2(v = 1) \overset{k_{VV1}}{\leftrightarrow} O_3(200) + N_2(v = 0) + 130 \text{ cm}^{-1} \tag{25}$$

$$O_3(000) + O_2(v = 1) \overset{k_{VV2}}{\leftrightarrow} O_3(100) + O_2(v = 0) + 456 \text{ cm}^{-1} \tag{26}$$

$$O_3(000) + O_2(v = 1) \overset{k_{VV3}}{\leftrightarrow} O_3(001) + O_2(v = 0) + 517 \text{ cm}^{-1} \tag{27}$$

$$O_3(102) + O_2(v = 0) \overset{k_{VV4}}{\leftrightarrow} O_3(000) + O_2(v = 2) - 4.9 \text{ cm}^{-1}. \tag{28}$$

A review of the rate coefficients for $k_{int1} - k_{int3}$ (internal conversion of vibrational energy), $k_{VT1} - k_{VT3}$ (V–T processes), and $k_{VV1} - k_{VV4}$ (V–V processes) is given in Manuilova and Shved (1992), Manuilova et al. (1998), and López-Puertas and Taylor (2001). The relation between the rate coefficients is the following: $k_{int1} \gg k_{int2} \approx k_{int3} \approx k_{VT1} \approx k_{VT2} \gg k_{VT3}$. Besides these processes and the radiative transitions shown in Fig. 11, the O_3 vibrational levels are populated in the process of chemical recombination of ozone in the presence of a third body:

$$O_2 + O(^3P) + M \rightarrow O_3(v_1, v_2, v_3) + M, \tag{29}$$
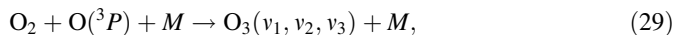
where M is N_2, O_2 or atomic oxygen. The energetics of this process is:
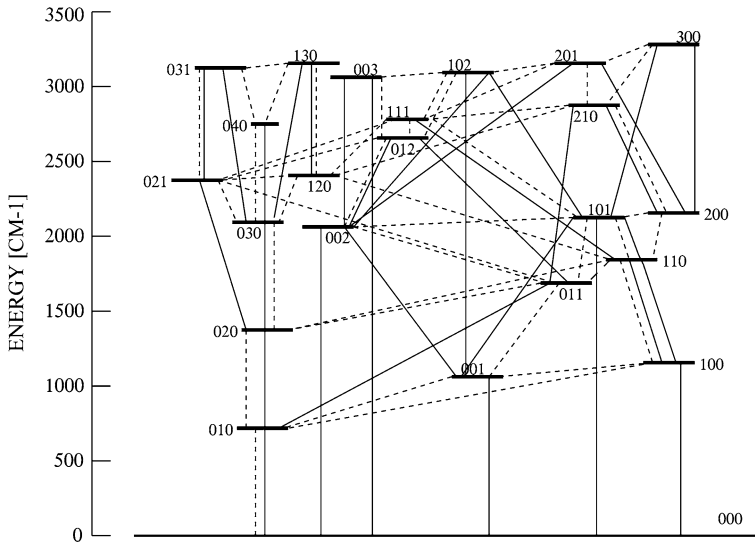
Fig. 11 Ozone molecule vibrational levels diagram (Manuilova et al. 1998). *Solid lines* optical transitions, *dashed lines* V–V and V–T transitions

$$\Delta H_f^0(O_2) + \Delta H_f^0(O(^3P)) = \Delta H_f^0(O_3) + E_{\text{vib}} + E_{\text{transl}} \qquad (30)$$

$$E_{\text{vib}} + E_{\text{transl}} = 106.5\,\text{kJ/mol} = \,\sim 8,900\,\text{cm}^{-1}, \qquad (31)$$

where ΔH_f^0 is the enthalpy of formation of gas at standard conditions, E_{vib} is the vibrational energy of O_3, and E_{transl} is the total translational (kinetic) energy of O_3 and M. The values of $\Delta H_f^0(O_2)$, $\Delta H_f^0(O(^3P))$, and $\Delta H_f^0(O_3)$ used for estimating $E_{\text{vib}} + E_{\text{transl}}$ in (30) were taken from the NIST Standard Reference Database (http://webbook.nist.gov/chemistry/).

As one can see from (31), the chemical energy released in the recombination process (29) can populate the O_3 vibrational levels up to its dissociation limit. In reality, the fractioning between the E_{vib} and E_{transl} is complicated. Several models have been suggested for the nascent E_{vib} distributions. In a widely used "zero surprisal" model (e.g., see Levine and Bernstein 1974; Gil-López et al. 2005), it is assumed that only $O_3(0, 0, v_3)$ levels are excited with the probability given by the formula:

$$f(v) = \frac{(1 - E_v/D_e)^{1.5}}{\sum_{v=1}^{7}(1 - E_v/D_e)^{1.5}}, \qquad (32)$$

where v and E_v are the level number and energy of v_3, respectively, and D_e is the dissociation energy. In other models (see Kaufmann et al. 2006), it is considered that all the excitation goes to a single level $v_3 = 3$, 5, or 8. Fernandez et al. (2009, 2010) assume that the branching ratio between the E_{vib} and E_{transl} is 7:3 and that the vibrational excitation energy goes to $v_3 = 6$. One can also assume that the chemical energy of the reaction (29) is used to excite the $O_3(v_1, v_2, v_3)$ levels near the dissociation limit (the so-called "Top-8" model in López-Puertas and Taylor 2001).

The comparison of the effects of the nascent distribution model on the $O_3(v_3)$ levels population is given in López-Puertas and Taylor (2001, Ch. 7.3.6, p. 211) where the vibrational temperatures for the first 7 v_3 levels obtained with the zero surprisal model are

compared with that obtained with "Top-8" model where the excitation is distributed among the uppermost vibrational levels below the dissociation limit. The study shows the high sensitivity of the corresponding v_3 level populations to the model chosen. In the zero surprisal model, the atmospheric emission from the low v_3 levels is higher compared to that in the "Top-8" model and vice versa, the emissions from the high v_3 levels in the zero surprisal model are lower than that in the "Top 8" model. We have to stress here that if one assumes that the process (29) populates the O_3 levels close to the dissociation limit, then the rate coefficients for the processes (19)–(24) need to be determined since the rate coefficients $k_{int1} - k_{int3}$ and $k_{VT1} - k_{VT3}$ cannot be applied to high-energy levels due to anharmonicity of the vibrations and due to the complicated physics of closely spaced vibrational levels.

The uncertainty of the nascent population model is currently the most challenging problem for the interpretation of O_3 radiation measured in the hot bands (Manuilova, private communication, 2012). For example, if the O_3 VMR profile is retrieved from the radiation in the (010–000), (100–000) and (001–000) transitions that are less sensitive to the nascent populations model and then used for the interpretation of the 4.8-μm hot bands radiation measurements (see Kaufmann et al. 2006), an inconsistency arises: the calculated 4.8-μm radiation is 2–3 times lower than the measured one in the 50–75 km altitude interval. Correspondingly, Kaufmann et al. (2006) had to assume that either the ozone is formed at the levels around 3,000 cm^{-1} (levels 003, 102, 201, or 300), like Manuilova et al. (1998) did, or that the k_{int2}, k_{int3} rate coefficients for hot band transitions have to be reduced by a factor three or four to fit the MIPAS measurements. From the point of view of the infrared energy budget, the branching ratio between the E_{vib} and E_{transl} energies is noteworthy since the latter term directly adds to the atmospheric heating while the E_{vib} is partially radiated back to the atmosphere and partially quenched and transformed to translational energy. This contribution to the heat reservoir may be found only by detailed solution of the non-LTE problem which accounts for the emission, propagation, absorption and re-distribution of radiative energy.

Figure 12 shows the vibrational temperatures of the (100) and (001) vibrational levels for the daytime and nighttime conditions calculated using the model of Manuilova et al. (1998). For most of the atmospheric scenarios, the breakdown of LTE for these levels starts at ∼65–70 km altitude. The vibrational temperatures shown in Fig. 12 are higher than the kinetic ones because of the recombination process (29) and the radiative pumping of the (100) and (001) levels by the absorption of radiation coming from the lower atmospheric layers and from the ground. The daytime increase of the vibrational temperatures shown in Fig. 12 is explained by a combined effect of higher daytime atomic oxygen VMR, higher O_3 VMR at 30–40 km, and lower O_3 VMR in the 50–75 km altitude interval.

The radiative pumping effects can be seen in Fig. 13 which shows that the net radiative effect of O_3 in the MLT area is heating that maximizes at ∼95 km altitude and varies from ∼0 K/day for the daytime cases to 3.0 K/day for the nighttime scenarios. Low absolute values of the net heating by O_3 in the MLT during daytime are explained by low O_3 VMRs (see solid lines in Fig. 6b). The energetic effects of ozone photolysis and subsequent energy transformation processes in the system of electronic-vibrational oxygen energy levels $O_2(b^3\Sigma_g^+, v)$, $O_2(a^1\Delta_g, v)$, and $O_2(X^3\Sigma^-, v)$ will be considered in the next section.

3.3 Molecular Oxygen and Ozone Photolysis

Absorption of solar ultraviolet radiation by O_2 and O_3 in the MLT leads to a whole chain of energy conversion processes. The first commonly accepted model of electronic kinetics of
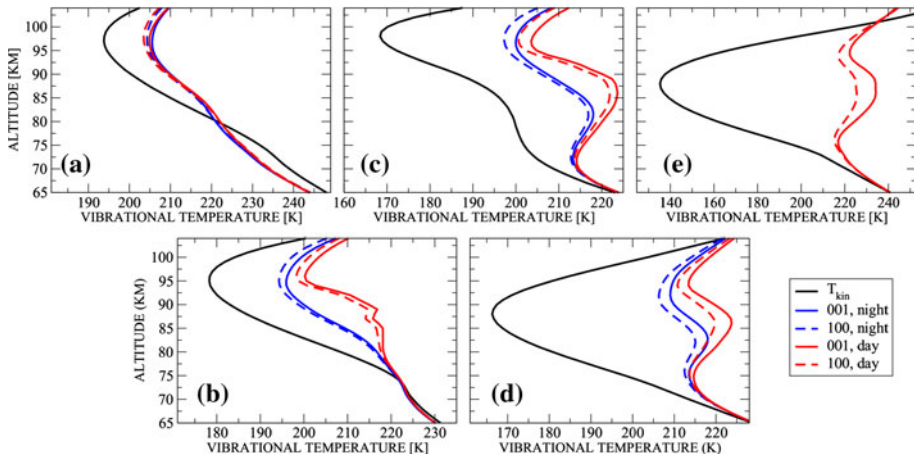
Fig. 12 Nighttime and daytime (twilight for the SAW case) populations of $O_3(100)$ and $O_3(001)$ vibrational levels in a form of vibrational temperatures for the five test atmospheres: (**a**) SAW, (**b**) MLW, (**c**) TROP, (**d**) MLS, (**e**) SAS

O_2/O_3 photolysis products was developed by Harris and Adams (1983) and Thomas et al. (1984) and was significantly improved by Mlynczak et al. (1993). Later, this model was substantially extended by Yankovsky and Manuilova (2006). The updates and optimizations of this model may be found in Yankovsky and Babaev (2010) and Yankovsky et al. (2011). In this section, we will refer to the model of Yankovsky and Manuilova (2006) and demonstrate its coupling with the system of vibrational levels presented in Fig. 4.

The upper panel of Fig. 14 shows that the molecular oxygen photolysis caused by absorption of radiation in the Schumann-Runge continuum (175–205 nm) and Lyman-alpha (Ly-α) line leads to producing the electronically excited oxygen atoms $O(^1D)$. These atoms are also produced as a result of O_3 photolysis in the Hartley band (200–310 nm). The collisions of $O(^1D)$ with molecular oxygen in the ground electronic state, $O_2(X^3\Sigma^-, 0)$, and the transfer of its electronic energy to O_2 give rise to the populations of electronically vibrationally excited molecular oxygen $O_2(b^3\Sigma_g^+, v)$ with the subsequent redistribution of excitation energy to $O_2(a^1\Delta_g, v)$ and $O_2(X^3\Sigma^-, v)$ electronic-vibrational levels. These levels are also directly populated by O_3 photolysis in the Hartley band, Huggins bands (310–350 nm), and Chappuis bands (410–750 nm) and by resonance absorption of solar radiation at 762, 689, 629 nm and 1.27 μm. At each electronic-vibrational level, the deposited energy can be either quenched by a collision with one of the atmospheric species (mainly with N_2, O_2, and O) or radiated to the atmosphere. The net effect of solar absorption leading to O_2/O_3 photolysis is heating (h_{O_2/O_3}) since the energy is deposited in the respective region, and only part of it escapes through radiation in the 1.27 μm and 762 nm O_2 bands (see the cooling components in Fig. 15). The total energy budget of O_2/O_3 photolysis may be represented in the following form:

$$
h_{O_2,O_3}(z) = \frac{1}{C_p(z)\rho(z)}
$$
$$
\times \left[\int_{\lambda_{a1}}^{\lambda_{a2}} E_a(\lambda)\Phi_{sol}(\lambda,z)\sigma_a(\lambda)d\lambda + \int_{\lambda_{b1}}^{\lambda_{b2}} E_b(\lambda)\Phi_{sol}(\lambda,z)\sigma_b(\lambda)d\lambda - \sum_i h\nu_i\Phi_i(z) \right],
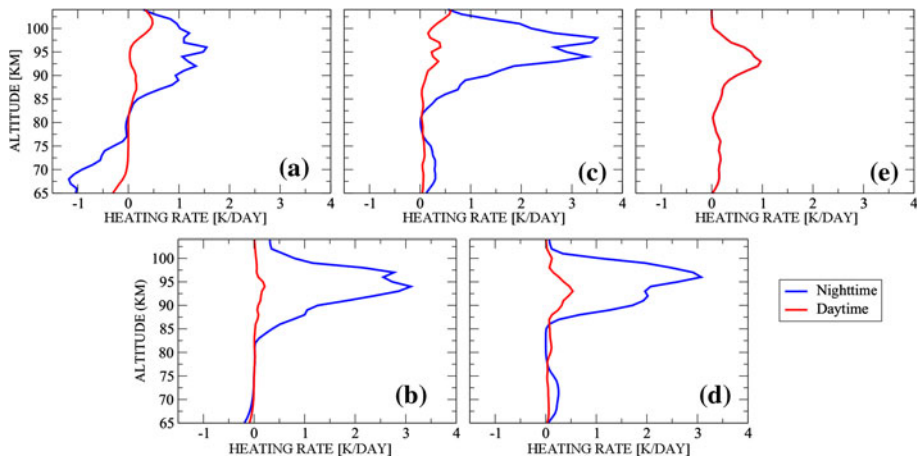$$

$$(33)$$

Fig. 13 Nighttime and daytime (twilight for the SAW case) net heating rates of ozone in the MLT region for the five test atmospheres: (**a**) SAW, (**b**) MLW, (**c**) TROP, (**d**) MLS, (**e**) SAS

where $C_p(z)$ is the air heat capacity at constant pressure, $\rho(z)$ is the density, the indices a and b are related to O_2 and O_3 photodissociation, respectively, $E(\lambda)$ is the energetic effect of one photodissociation act calculated from the energy of the absorbed quantum and ΔH_f^0 values of the participating atoms and molecules, and the amount of $\Phi_{sol}(\lambda, z)$ is the incoming solar flux for wave length λ at the altitude z, $\sigma(\lambda)$ is the absorption cross section, $\Phi_i(z)$ and $h\nu_i$ are the integrated volume emission rates at the altitude z and the energies of emission quanta that correspond to 630, 629, 689, 762, and 1.27 μm radiation (Fig. 14, upper panel).

Cross-sections for O_2 photodissociation have been the subject of numerous laboratory studies. Based on these studies, the parameterization schemes and tables for different spectral areas have been built: see Chabrillat and Kockarts (1997) for Ly-α radiation absorption; Minschwaner et al. (1992) and Kockarts (1994) for O_2 absorption in Schumann-Runge bands (175–205 nm); Nee and Lee (1997) and DeMajistre et al. (2001) for the absorption in Schumann-Runge continuum. Regarding the O_3 absorption cross-sections one can refer to: DeMore et al. (1997) for the absorption in Hartley band; Malicet et al. (1995) for Huggins bands; Brion et al. (1998) for Chappuis bands. The estimates of terms in (33) for the heating by the absorption of the UV solar radiation by O_2 and O_3 and for the 1.27 μm and 762 nm bands cooling (main cooling terms in (33)) are shown in Fig. 15. The cooling component is calculated from the 762 nm and 1.27 μm $\Phi_i(z)$ fluxes measured in the METEORS experiment (see Mlynczak et al. 2001). Heating rates due to O_2 and O_3 photodissociation for tropical conditions were estimated by Fomichev (2009) using the method suggested by Mlynczak and Solomon (1993) and Mlynczak and Marshall (1996). Overall, the net MLT heating due to photochemical effects of solar radiation on O_2 and O_3 is quite significant and can reach values of about 8 K/day at $\sim$95 km altitude. At the same altitude, both O_2 bands provide significant cooling of about 3.5 K/day.

The model of the O_2/O_3 photolysis product kinetics shown in the upper panel of Fig. 14 is implemented in the ALI-ARMS code (see Sect. 2.3). It allows simultaneous self-consistent solution of the non-LTE problem for the set of vibrational levels of molecules (Fig. 4) and the system of electronic-vibrational levels of the O_2 and O_3 molecules and electronic levels of O atoms. The coupling of the O_2/O_3 system of levels of Fig. 14 with
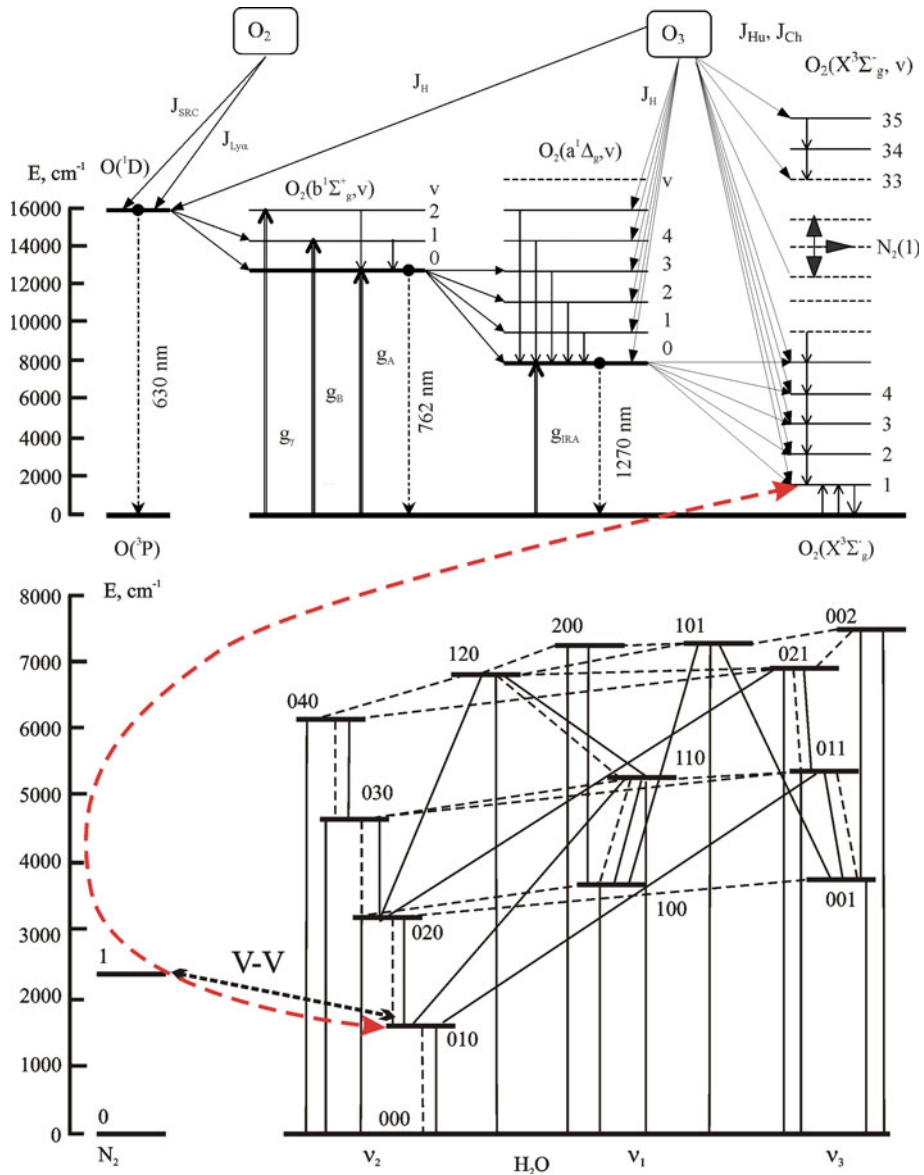
Fig. 14 Joint scheme of O_2/O_3 photolysis products kinetics (*upper panel*, after Yankovsky and Manuilova (2006)) and H_2O vibrational levels (*lower panel*). In the *upper panel thick horizontal lines* correspond to electronic states of atomic and molecular oxygen; *thin horizontal lines* represent the vibrational substructure of the corresponding electronic state; *lines* with *arrows* in the *upper* part of the panel denote the O_2 and O_3 photolysis after absorption of radiation in the Schumann-Runge continuum (J_{SRC}), Lyman-α line ($J_{Ly\alpha}$), Hartley (J_H), Huggins (J_{Hu}), and Chappuis (J_{Ch}) bands (see text for more details). In the *lower panel thick horizontal lines* correspond to vibrational states of the H_2O molecule; optical transitions are shown as *thin solid lines*; *dashed lines* represent V–T processes, and *thick dashed lines* with *arrows* correspond to V–V energy exchange processes. Note the V–V coupling of the O_2 (X, v = 1) level in the *upper* panel and $H_2O(010)$ level in the *lower* panel
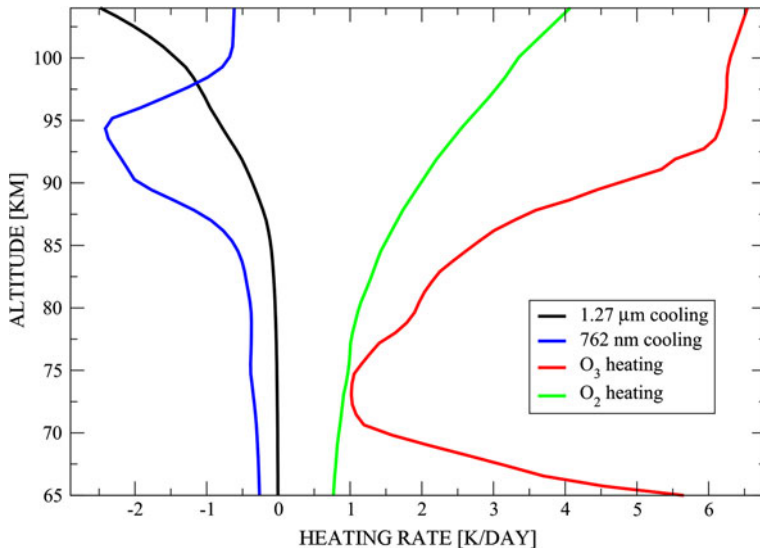
Fig. 15 Heating effects due to solar absorption by O_2 (Lyman-α, Schumann-Runge bands, and Schumann-Runge continuum) and O_3 (Hartley, Huggins, and Chappuis bands) after Fomichev (2009). Cooling in the 1.27 μm and 762 nm bands is estimated from the corresponding volume emission rates measured by the METEORS experiment (Mlynczak et al. 2001)

the molecular levels shown in Fig. 4 is realized through the V–V exchanges. In addition, the photochemical model is linked to the system of molecular levels shown in Figs. 2 and 4 through the $O(^1D)$ energy transfer to $N_2(v)$ vibrational levels, which are also pumped from the OH(v) during nighttime. The V–V exchange between $O_2(1)$, $N_2(1)$ and $H_2O(010)$ shown in Fig. 14 dominates among these energy transfers and is important for the H_2O model discussed in the next section.

3.4 Water Vapor

Water vapor cools the atmosphere in rotational and vibrational bands. The direct energetic effect of H_2O on the MLT cooling is tertiary, compared to that of CO_2 and O_3. However, besides the direct effects of infrared cooling, H_2O influences the composition and energy budget of the MLT area in a number of ways. Being a source for chemically active constituents, such as OH, $O(^1D)$, H_2, and H (e.g., see Brasseur and Solomon 2005), it participates in the so-called "zero-cycle" reactions where the absorption of solar short-wave radiation leads to H_2O photodissociation with subsequent recombination in a number of processes that result in heating of the atmosphere (e.g., see Sonnemann et al. 2005). The existence of water molecules at sufficiently low temperatures near the polar summer mesopause leads to the nucleation of ice particles in the MLT region (e.g., see Rapp and Thomas 2006, and references therein). These particles are responsible for such phenomena as noctilucent clouds (NLCs) and polar mesospheric summer echoes (PMSEs). Because of high sensitivity to local kinetic temperatures, the NLC and PMSE phenomena can be used as temperature probes for these regions (e.g., see Lübken et al. 2007; Petelina and Zasetsky 2009) and as possible indicators of climate change (e.g., see Thomas 2003).

In the gas phase, water molecule vibrations involve combinations of symmetric stretch (v_1), covalent bond bending (v_2), and asymmetric stretch (v_3) modes with the band strength

ratio for the fundamental bands of the main H_2O isotope being 0.07/1.50/1.00 for the ν_1, ν_2, and ν_3 vibrations, respectively (e.g., see Goody and Yung 1995, and references therein, and Rothman et al. 2009). The diagram in the lower panel of Fig. 14 shows the ground level and various excited vibrational levels of the H_2O molecule up to 7,445 cm^{-1}. The levels are marked in accordance with the number of vibrational quanta $\nu_1\nu_2\nu_3$. The rotational levels of H_2O are considered to be in LTE in the MLT while the vibrational levels start deviating from LTE above ~ 50 km. The detailed description and sensitivity studies for the H_2O non-LTE model may be found in López-Puertas and Taylor (2001), Manuilova et al. (2001), and Feofilov et al. (2009). The highest sensitivity of the $H_2O(\nu_2)$ vibrational levels population is to the rate coefficient k_{VV} of the V–V exchange process:

$$H_2O(\nu_2) + O_2(X^3\Sigma^-, 1) \xrightarrow{k_{VV}} H_2O(\nu_2 + 1) + O_2(X^3\Sigma^-, 0). \qquad (34)$$
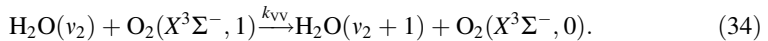
This sensitivity is bilateral: $O_2(X^3\Sigma^-, 1)$ is pumped in a series of processes shown in the upper panel of Fig. 14 and reducing the value of the k_{VV} coefficient may lead to a decrease in $H_2O(\nu_2)$ pumping. On the other hand, $O_2(X^3\Sigma^-, 0)$ serves as a vibrational energy "reservoir" for $H_2O(\nu_2)$ quanta; reducing the k_{VV} leads to decoupling of $H_2O(\nu_2)$ system from this reservoir and to an increase of $H_2O(\nu_2)$ populations. This issue is especially important when dealing with the interpretation of 6.6 μm H_2O radiation that will be described in Sect. 5.2.2. The k_{VV} value estimated by different groups varies from 5.5×10^{-13} cm^3 s^{-1} (see Huestis 2006) through 1.0×10^{-12} cm^{3}s^{-1} (see Koukouli et al. 2006) and 1.2×10^{-12} cm^3 s^{-1} (see Feofilov et al. 2009) to 1.7×10^{-12} cm^3 s^{-1} (see García-Comas et al. 2002); see also Table 2 in Feofilov et al. (2009) for a historical review of this rate coefficient.

Figure 16 shows the contributions of the main isotope H_2O rotational band (associated with the ground vibrational level) and vibrational bands to radiative heating of the MLT. As one can see, the net effect of the radiative transfer in the vibrational band in this region is heating since H_2O absorbs the radiation coming up from below where the net radiative effect is cooling (not shown in the figure due to the selected vertical axis limits). The vibrational band is responsible for a maximum of 0.5 K/day at ~ 70 km altitude for the MLS and SAS profiles. On the other hand, the rotational band cools the mesosphere at 70–80 km and provides 0.6–1.5 K/day cooling in its maximum. It is interesting to note both quantitative and qualitative differences between the rotational cooling profiles for the SAW, MLW, TROP and MLS, SAS atmospheric scenarios. For the latter two, the cooling in the cold mesopause is compensated by absorption of the radiation coming from below. Summing up the profiles of the vibrational and rotational heating rates leads to reduction of the cooling effect of the rotational band in the 75–85 km altitude range to 1.5 K/day for the SAW, 1.1 K/day for the MLW and the TROP, 0.5 K/day for the MLS, and 0.2 K/day for the SAS atmospheric scenario. Above ~ 85 km altitude, the H_2O contribution to the MLT energy budget becomes negligible for the SAW, MLW, TROP, and MLS scenarios due to the rapidly decreasing H_2O VMR. For the SAS atmosphere, the rotational band cooling at 100 km altitude remains on the order of 0.5 K/day due both to higher SAS temperatures here and higher summer H_2O VMR that is explained by the upward transport by vertical winds (see Garcia and Solomon 1994; Körner and Sonnemann 2001).

3.5 Radiative Cooling of the MLT Associated with Gravity Wave-Induced Atmospheric Fluctuations

An interesting aspect of the radiative cooling in the MLT is the combined effect of the small-scale fluctuations in the atmospheric vertical structure, and radiative transfer in the
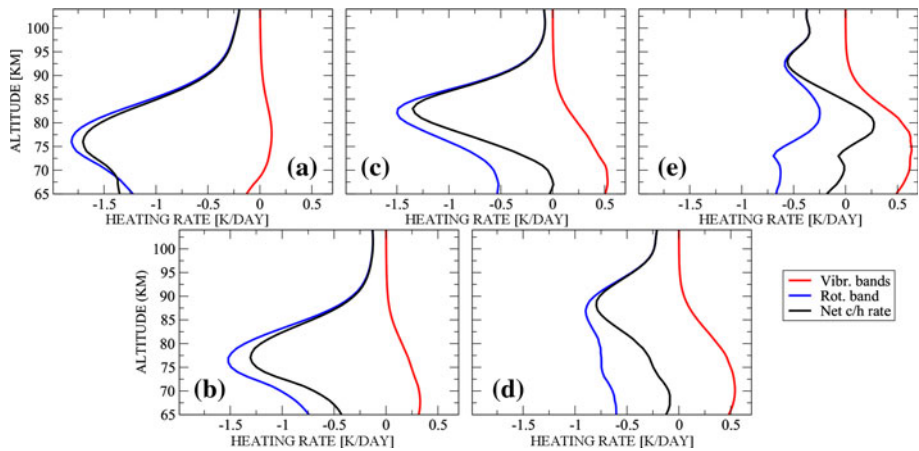
Fig. 16 Net heating rates of H_2O in vibrational bands and in the rotational band for the five daytime test atmospheres: (**a**) SAW (twilight), (**b**) MLW, (**c**) TROP, (**d**) MLS, (**e**) SAS

15 μm CO_2 band. First described by Kutepov et al. (2007) for $T(z)$ variations, it was later extended to the variation of $T(z)$, $CO_2(z)$, and $O(^3P)(z)$ distributions (see Kutepov et al. 2012). The additional cooling in the MLT caused by this phenomenon is comparable with the heating effects of O_3 and H_2O, so we go into some detail regarding its mechanism. As one can see from the Sect. 3 of this work, the heating rates in the atmosphere strongly depend on the distributions of temperature and of radiatively active atmospheric components.

In the middle atmosphere, instantaneous profiles are highly irregular due to disturbances associated with gravity waves (GWs). The GW amplitude increases with height and the r.m.s. of temperature fluctuations is about 20 K at 90 km altitude (e.g., see Whiteway and Carswell 1995; Smith 2012). The wavelengths $\lambda \ll 2\pi H$, where H is a scale height, are usually not well resolved in modern GCMs, and the dynamic effects of these "sub-grid" GWs are usually taken into account in the form of a "GW drag" parameterization (see Fritts and Alexander 2003). On the other hand, the atmospheric parameter fluctuations caused by GWs affect the radiative transfer and the corresponding heating rates. These effects, however, are usually omitted in GCMs because (a) small-scale GWs are not well resolved and (b) radiative heating rates $h(z)$ parameterizations (see also Sect. 4) utilize a grid coarser than the grid of the GCM.

In the MLT, the trace gases CO_2 and $O(^3P)$ can be considered as conservative tracers so that the GW-induced variations are entirely due to adiabatic displacements of air parcels. In this case, one can express the trace gas VMR variation, ζ', as a function of temperature variation T':

$$\zeta' = \gamma T', \quad \gamma = \frac{d\zeta}{dz} \cdot \left(\frac{dT}{dz} + \frac{RT}{c_p H}\right)^{-1}, \tag{35}$$

where ζ is the mean VMR, T is the mean temperature profile, and R is the gas constant. If the model for T' fluctuations is known, one can perform a numerical experiment to identify the effects of GW-induced fluctuations on mean radiative heating rate. This experiment was carried out for the five atmospheric scenarios. For each case, 1,000 individual GWs were generated in accordance with the statistical model described in Kutepov et al. (2007).

The ζ' values were calculated in accordance with (35), and the non-LTE problem was run for each of the individual atmospheric profiles of T, $O(^3P)$, and CO_2. After that, the differences of the heating rates $\Delta h(z) = \bar{h}(z) - h_{\text{aver.atm.}}(z)$ were calculated where $\bar{h}(z)$ represents the $h(z)$ averaged over 1,000 profiles and $h_{\text{aver.atm.}}(z)$ is the heating rate calculated for an averaged atmospheric profile. The r.m.s. profile of the temperature fluctuations $\sigma_T = \left[\frac{1}{N}\sum_{i=1}^{N}(T_i')^2\right]^{1/2}$ for SAW atmospheric scenario is shown in Fig. 17a. The results presented in Fig. 17b show the combined effect of T, $O(^3P)$ and CO_2 fluctuations on the CO_2 radiative heating. As one can see, the main effect of GW-induced fluctuations is an additional cooling of up to 3 K/day (for SAW and MLW) in the altitude region 80–95 km and a slight additional warming up to 1 K/day (for MLS). The observed effect is mainly related to temperature fluctuations and is explained by increased mean local thermal emission with respect to emission for the non-disturbed temperature due to strong non-linear temperature dependence of the Planck function (see Kutepov et al. 2007). Accounting for ζ_{CO_2} and $\zeta_{O(^3P)}$ fluctuations leads to changes in $\Delta h(z)$ compared to the results obtained in Kutepov et al. (2007): $\zeta_{O(^3P)}$ fluctuation increases the additional cooling in the 85–100 km area by a maximum of ~ 1 K/day (SAW) while the ζ_{CO_2} fluctuation has the opposite effect, decreasing the $h(z)$ in 88–100 km by ~ 1.7 K/day. These effects and their signs are related to ζ gradients in the MLT: according to (35), large ζ gradients lead to large ζ' values, and in the MLT the $\zeta_{O(^3P)}$ rapidly increases with height while the ζ_{CO_2} decreases with height (see Fig. 6a, d, respectively).

A more detailed explanation for the $\Delta h(z)$ behavior with respect to temperature, ζ_{CO_2}, and ζ_{O_3} fluctuations as well as its parameterization with respect to average temperature variation σ_T, and $\zeta_{CO_2}(z)$ and $\zeta_{O(^3P)}(z)$ distributions is given in Kutepov et al. (2012) who show that the net effect of these fluctuations can cause an additional cooling of up to 4 K/day near the mesopause.

4 Optimization of Heating Rate Calculation for GCMs

Let us assume that there are N_V vibrational levels involved in the problem and that the atmosphere is discretized at N_D altitude grid points. Solving the steady state equations (8) for this system requires solving the radiative transfer equation (4) for N_R spectral lines in the N_B ro-vibrational molecular bands. In the LBL approach for the non-overlapping lines, each line must be resolved in N_F frequency points to include the changes of the line shape with respect to atmospheric pressure and temperature. The above-mentioned parameters in modern models for molecules considered above are of the following order: $N_V = 10 - 100$, $N_D \approx 100$, $N_B = 10 - 1,000$, $N_R = 100 - 10^5$, $N_F = 10 - 100$. Naturally, the exact non-LTE calculations performed in this manner cannot be used to estimate the heating rates $h(z)$ in GCMs. Instead, the $h(z)$ in molecular bands are usually calculated with the help of some parameterizations that take into account the main physical mechanism responsible for the radiative cooling or heating for each particular molecule. Obviously, there is a trade-off between accuracy and efficiency of these algorithms, most of which are described in the review paper of Fomichev (2009). Among these methods, one has to highlight the CO_2 infrared cooling parameterizations by Fomichev et al. (1993) and Fomichev et al. (1998a), which cover both LTE and non-LTE region starting from 15 km up to the altitudes in thermosphere. The non-LTE fraction of this algorithm (see Kutepov and Fomichev 1993)
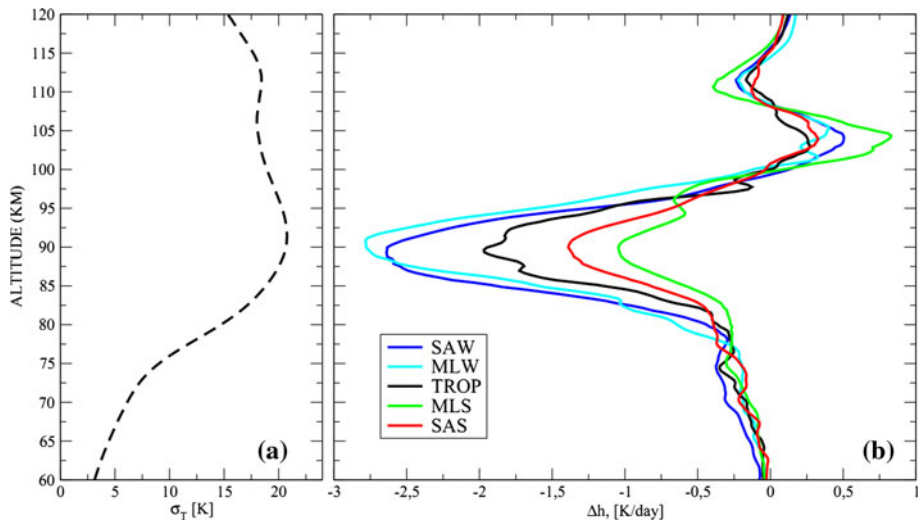
Fig. 17 Additional cooling caused by atmospheric vertical structure fluctuations associated with gravity waves. (**a**) r.m.s. of the temperature variation caused by gravity waves for the SAW atmospheric scenario; (**b**) net effect of T(z), CO_2(z), and O(z) variations on heating of the MLT region for the five test atmospheres: (a) SAW (twilight), (b) MLW, (c) TROP, (d) MLS, (e) SAS

evolved from the second-order escape probability approximation of Frisch and Frisch (1975) and was later supplemented by the parameterization of heating by the CO_2 absorption of the near-infrared solar radiation (see Fomichev et al. 2004). The accuracy of this method in the MLT region is reported to be about 1 K/day if $k_{VT} = 1.5 \times 10^{-12}$ cm^3 s^{-1} is utilized (see Fomichev 2009).

The 9.6 μm O_3 cooling effects have not been parameterized yet due to the complexity of the O_3 non-LTE model and its relatively small effect during the day. The same is also true for H_2O. However, during the nighttime, the contribution of O_3 to the MLT energy budget becomes noticeable (up to +3 K/day at ~95 km altitude, see Fig. 13), which calls for its parameterization in the GCM. The absence of this term might create a negative temperature bias at 85–100 km altitude.

Because of the increasing requirements for accuracy and flexibility of the radiative heating estimates in GCMs, it is unlikely that the parameterizations based on different approximate treatments of the non-LTE radiative transfer like various order escape probability approximations or matrix approaches (see Fomichev et al. 1993, 1998a) will satisfy the users. On the other hand, computer processor capacities as well as those of multi-core and parallel processing computers are continually increasing. This is supplemented also by the dramatic progress in the efficiency of exact multiple scattering non-LTE radiative transfer algorithms (see Gusev and Kutepov 2003).

This allows turning from developing the radiative cooling parameterizations for GCMs to utilizing the exact non-LTE radiative transfer algorithms. Below, we describe an approach developed first for calculating $h(z)$ in the 15 μm CO_2 bands in the Martian atmosphere (see Hartogh et al. 2005, Feofilov et al. 2006) and apply it to the terrestrial atmosphere. Since this scheme is based on our exact reference non-LTE model and the ALI-ARMS code, it is potentially applicable to any significant atmospheric molecule in the planetary atmosphere, given that the non-LTE reference model for this molecule exists.

The acceleration approach consists of the three steps: (a) applying the ALI (for Accelerated Lambda Iteration) technique for radiative transfer; (b) replacing the radiative transfer in the N_R individual lines of the N_B molecular bands by radiative transfer in the molecular bands themselves by utilizing the opacity distribution function (ODF) method; and (c) reducing the N_V involved into the steady-state Eq. (8). The peculiarities of each step are discussed below.

4.1 Methods of Solving the Non-LTE Problem: The ALI Technique

The most straightforward way of solving the joint system of the SSE (8) and the RTE (4) is to iterate between them. This approach is traditionally called the "lambda iteration" (LI) and has been studied in detail in the astrophysical context since the 1920s (see Unsöld 1968). In atmospheric science, the straightforward application of this technique was described by Wintersteiner et al. (1992). This approach numerically simulates the multiple scattering of photons and is attractive since it involves N_D matrices of $N_V \times N_V$ size. However, as Kutepov et al. (1998) showed, the convergence of the LI method is slow since the photons are "trapped" in the cores of optically thick lines. Kutepov et al. (1998) and Gusev and Kutepov (2003) studied the LI approach in detail for non-LTE problems in the Earth's and planetary atmospheres and demonstrated that its convergence rate could be so slow that false solutions appear to be stable and/or the accumulation of numerical errors causes the process to diverge. They showed that the LI approach is particularly inefficient for the solution of the non-LTE problem in molecular bands, like those, for instance, for CO_2 in the Earth's and Martian atmospheres, since the general non-local and nonlinear nature of the non-LTE problem is aggravated here by the additional nonlinearity introduced by the V–V energy exchanges whose rates depend on the products of level populations.

An alternative way of solving the non-LTE problem is treating the SSE (8) and the RTE (4) simultaneously by discretizing the RTE with respect to an optical depth or pressure grid to get a matrix representation of the radiative terms in the SSE. In this approach (see, e.g., López-Puertas and Taylor 2001; Funke et al. 2012), the non-local radiative terms are expressed in terms of populations and the problem is solved iteratively as a set of non-local linear problems. The convergence of this method is usually fast (see Gusev and Kutepov 2003), but the time for filling out and inverting the matrices is large because of their size $(N_V \times N_D) \times (N_V \times N_D)$. From the point of view of computation time, one matrix iteration is roughly equivalent to N_D lambda iterations. However, if both N_D and N_V are large, each matrix iteration is very expensive in computer time; the same result may be achieved faster with LI or its accelerated version discussed below.

The problems related to the application of standard LI or matrix approaches outlined above are overcome by utilizing the so-called "accelerated lambda iteration" (ALI) method developed in stellar astrophysics (see Rybicki and Hummer 1991, 1992 and references therein). The family of ALI methods is based on the operator splitting of the form $\Lambda = \Lambda^* + (\Lambda - \Lambda^*)$, where Λ is the monochromatic lambda operator $\Lambda_{\mu v}$ along the ray with direction μ defined by the formal solution of the RTE (4) $I_{\mu v} = \Lambda_{\mu v}[S_v]$, where $S_v = \eta_{\mu v}/\chi_{\mu v}$ is the source function and the square brackets mean "acting on". The splitting of the operator leads to the following iteration scheme: $I_{\mu v}^i = \Lambda_{\mu v}^{*i-1}[S_v^i] + (\Lambda_{\mu v}^{i-1} - \Lambda_{\mu v}^{*i-1})[S_v^{i-1}] = \Lambda_{\mu v}^{*i-1}[S_v^i] + I_{\mu v}^{\text{eff } i-1}$, where i and $i-1$ indices denote the current and the previous iterations, respectively, and $I_{\mu v}^{\text{eff } i-1} = (\Lambda_{\mu v}^{i-1} - \Lambda_{\mu v}^{*i-1})[S_v^{i-1}]$ is the "effective" intensity. Although this equation is only approximate at each iteration, it becomes exact for the converged solution, for which

$S_v^i = S_v^{i-1}$, $\Lambda_{\mu v}^{*i} = \Lambda_{\mu v}^{*i-1}$, and $\Lambda_{\mu v}^i = \Lambda_{\mu v}^{i-1}$. This iteration scheme describes a whole class of methods, each specified by the choice of a particular approximate lambda operator $\Lambda_{\mu v}^*$. The simplest choice is to use the diagonal part of the matrix representation of the exact lambda operator as it is done in the ALI-ARMS research code. Using a "preconditioning" approach (see Rybicki and Hummer 1991, 1992), one can rewrite the radiative rate coefficients in such a way that much of the transfer in the optically thick "core" of the line, described by the local part of the lambda operator, is canceled analytically: $R_{ll'}^{\text{eff}} = A_{ll'}(1 - \Lambda_{ll'}^{*i-1}) + B_{ll'}\bar{J}_{ll'}^{\text{eff }i-1}$, where $\Lambda_{ll'}^*$ and $\bar{J}_{ll'}^{\text{eff}}$ are obtained from $\Lambda_{\mu v}^*$ and $I_{\mu v}^{\text{eff}}$ by applying double integration $1/4\pi \int d\mu \int \phi_{ll'}(v)dv$. As a result, the ALI method converges much faster than the LI method while it still utilizes N_D matrices of $N_V \times N_V$ size. The convergence speed of LI, matrix, and ALI methods has been studied in detail by Kutepov et al. (1998) who showed the superiority of ALI over the two other approaches for the atmospheres of Earth and Mars.

4.2 Optimizing the Radiative Transfer Calculations in Molecular Bands: Reducing the Number of Frequency Points

Additional significant computational time savings may be reached by optimizing the radiative transfer calculations. The latter linearly depends on the number of frequency and angle points in the angle and frequency integrals in (3). Whereas the number of angle points usually does not exceed 4, the number of frequency points is very large: the algorithm needs to treat the radiative transfer adequately in N_F points within each of N_R rovibrational lines for each of N_B bands considered. If one considers the $\eta(v)$ and $\chi(v)$ (see Eq. (10)) for a group of lines belonging to one molecular band branch and builds them using the contributions of N_R individual lines $\eta_{ll'}(v)$ and $\chi_{ll'}(v)$, one will obtain the "spectral profile" characterized by non-monotonic behavior. In order to evaluate the integral of type (3), one has to consider this profile for a large number of frequency points. One of the ways of optimizing the radiative transfer for a molecular band would be to reduce the N_R by retaining strong lines and omitting weak lines. However, this will barely help and may lead to undesirable results for optically dense media since in this case the radiative transfer occurs mostly in the weak lines and partly in the far wings of strong lines.

In the LTE area, the reduction of frequency points number is usually achieved by utilizing the so-called CKD (correlated k-distribution) method that is based on grouping the gaseous spectral transmittances in accordance with the absorption coefficient k. In this method, it is assumed that the k-distributions built for atmospheric layers with different pressure and temperature provide the spectral frequency correlation required for adequately reproducing the radiative transfer at any given frequency. In reality, the method appears to be accurate only in the case of radiative transfer between adjacent vertical levels or in the cases of low vertical temperature gradients. For flux calculations in the LTE area, it was found that the method is accurate to within 1 % (see Goody et al. 1989; Lacis and Oinas 1991; Fu and Liou 1992). However, the k-correlation scheme is not applicable in the case of non-LTE because the vibrational level populations involved in the building of k-distributions (and calculated in the LTE according to Boltzmann's law for a local temperature) are unknown and depend on the solution of RTE.

In the context of non-LTE, one may use the idea of opacity distribution function (ODF), as discussed by Anderson (1987) and Mihalas (1978). In this approach, the absorption cross section is re-sampled to yield a monotonic function of frequency that can be represented by a relatively small number of frequency points. Though the idea is similar to the k-correlation, in this method, the absorption and emission profiles and the populations are

treated separately, which allows accounting for the non-LTE conditions. There are two potential problems associated with this approach. First, the positions of the lines in the original and re-sampled $\chi(v)$ distributions may be not the same since the re-ordering depends on the rotational distribution function in the ro-vibrational band, which, in turn, depends on temperature. The second problem is linked with the overlapping of two or more different molecular bands. Fortunately, these issues have little effect on the populations of the vibrational levels and radiative cooling and heating rates. The first problem is efficiently masked by photon trapping in the cores of thick lines and by relatively small changes in the temperature from layer to layer. The effects of the second problem can be neglected due to the validity of the non-overlapping lines approximation for the majority of applications in the MLT (see López-Puertas and Taylor 2001).

Since the use of the ODF approach for treating molecular bands is new, we provide some background information on it. If one considers a simple case of the non-overlapping branches of molecular bands, one can write the opacity and emissivity distributions for these spectral "profiles" as

$$\eta_{vv'}^b(v) = \frac{hv_{vv'}}{4\pi} n_v A_{vv'}^b(T) \varphi_{vv'}^e(v) \tag{36}$$

$$\chi_{vv'}^b(v) = \frac{hv_{vv'}}{4\pi} \left[n_{v'} B_{v'v}^b(T) \varphi_{v'v}^a(v) - n_v B_{vv'}^b(T) \varphi_{vv'}^s(v) \right], \tag{37}$$

where $A_{vv'}^b(T)$, $B_{vv'}^b(T)$, and $B_{v'v}^b(T)$ are the temperature-dependent Einstein coefficients for the branch, and $\varphi_{vv'}^e(v)$, $\varphi_{vv'}^a(v)$, and $\varphi_{vv'}^s(v)$ are the normalized branch profile functions for emission, absorption, and stimulated emissions, respectively. We draw the reader's attention to the fact that, compared to the CKD approach, the vibrational levels populations do not enter these branch profile functions. These profile functions are highly non-monotonic since they are constructed as superpositions of individual line profiles presented by the Voigt functions and weighted with the normalized rotational distribution.

Let us now define the $\phi(v)$ functions as re-sampled and sorted $\phi_{vv'}(v)$ profiles and also define normalized distributions

$$\alpha(x) = \frac{1}{\phi(0)} \phi_{vv'} \left(\frac{1}{\phi(0)} x \right), \tag{38}$$

where $x = v \cdot \phi(0)$, and for which $\alpha(0) = 1$, $\int_0^{+\infty} \alpha(x) dx = 1$. We have built and analyzed several hundreds of these functions for linear molecules CO_2, N_2O and CO fundamental and hot branches for broad ranges of pressure and temperature variations ($P = 10^{-9} - 1$ bar, $T = 150-600$ K).

Two principal conclusions, which followed from this analysis, are:

1) $\varphi_{vv'}^e(v)$, $\varphi_{vv'}^a(v)$, and $\varphi_{vv'}^s(v)$ profiles for emission, absorption and stimulated emission of each branch nearly coincide (their relative differences do not exceed a few fractions of percent), and, therefore, may be represented by a single function $\alpha(x)$, which we will call "ODF cross section" or simply "ODF". Similar to the case of the complete frequency redistribution within a single line, when line absorption, emission, and stimulated emission in the line are described by the same Voight function, this effect can be called "complete frequency redistribution" within the branch.

2) For the majority of the considered molecular bands of various molecules, the ODF cross-sections $\alpha(x)$ for P, Q and R branches of perpendicular bands or those for P and

R branches of parallel bands are remarkably close. Although in the pressure and temperature ranges considered their relative differences in narrow intervals Δx may reach 25 %, this has no significant effect on estimation of integrals of type (3). It allows operating with the single ODF cross section $\alpha(x)$ for each branch of any band of any of the linear molecules considered.

If the shape of the $\alpha(x)$ profile is known, then the Eqs. (36) and (37) may be rewritten for $\phi(v)$, which is a monotonic function that can be represented in a small number of frequency (or better to say "pseudo-frequency") points N_F. This means that the ODF approach allows each branch to be replaced by a single "superline" of a special shape, which may be parameterized with respect to variations of pressure and temperature. Further analysis has shown that the "superline" can be approximated by a function similar to the Voigt function, in which $\exp(-y^2)$ is replaced by $\exp(-|y|)$.

The tests show that N_F required for the sufficient accuracy of the RTE calculations when applying ODF is approximately equal to the number of frequency points for a single line in the LBL approach. Therefore, the acceleration factor that can be reached by utilizing the ODF approach is roughly equal to the number of spectral lines within the branch (~ 100 for CO_2, $\sim 1{,}000$ for O_3). The accuracy of the ODF approach with respect to heating rate calculations is shown in Fig. 18. As one can see, the errors for the net heating rate in CO_2 do not exceed ± 0.15 K/day compared to the reference LBL data for all test atmospheres. This high accuracy of the radiative flux divergence calculations, which are extremely sensitive to the radiative transfer treatment, means that the ODF approach in its version outlined above significantly exceeds the CKD approach in its flexibility. Compared to CKD which provides reasonable accuracy only for adjacent atmospheric levels with low temperature gradient, the ODF approach demonstrates high accuracy over the wide altitude range of the MLT, where the temperature exhibits large changes with altitude.

We found that the higher accuracy of the ODF approach is explained by the much stronger dependence of the "superline" profile wing on temperature: the wing of the "superline" is proportional to T^{-1} while the single Voigt line wing is proportional to $T^{-1/2}$. This temperature dependence efficiently compensates for the differences between the ODF and LBL approaches, associated with the radiative energy exchange between distant atmospheric layers having different temperatures.

4.3 Reducing the Number of Levels

For any of the methods described in Sect. 4.1, the time required for solving the problem depends on N_V^2; thus, reducing the number of vibrational levels involved in the non-LTE problem is desirable. On the other hand, the vibrational levels are involved in complicated chains of V–V, V–T, and radiative transfer processes, so any optimization should be performed with particular care. We have investigated the accuracy of day- and nighttime $h(z)$ calculations with respect to the number of vibrational levels involved. This study performed for five test atmospheres shows that for daytime non-LTE models of CO_2 the reduced set of vibrational levels that guarantees the 1 K/day accuracy (which is a typical requirement of modern GCMs) even for high values of CO_2–O quenching rate $k_{VT} = 6.0 \times 10^{-12} \mathrm{cm}^3\,\mathrm{s}^{-1}$ (see Sect. 3.1.2) includes 15 excited levels, some of which (so called "super-levels") consist of vibrational levels closely spaced in energy and coupled by intensive intra-molecular V–V exchange. For these levels, we will use the notation ($v_{1,2}$, v_3) where $v_{1,2} = 2v_1 + v_2$. In this notation, the levels for 626-th isotope are: (1,0); (2,0); (3,0); (0,1); (4,0); (1,1); (2,1); (3,1); (4,1). For 636 and 628, the levels are (1,0); (2,0); and
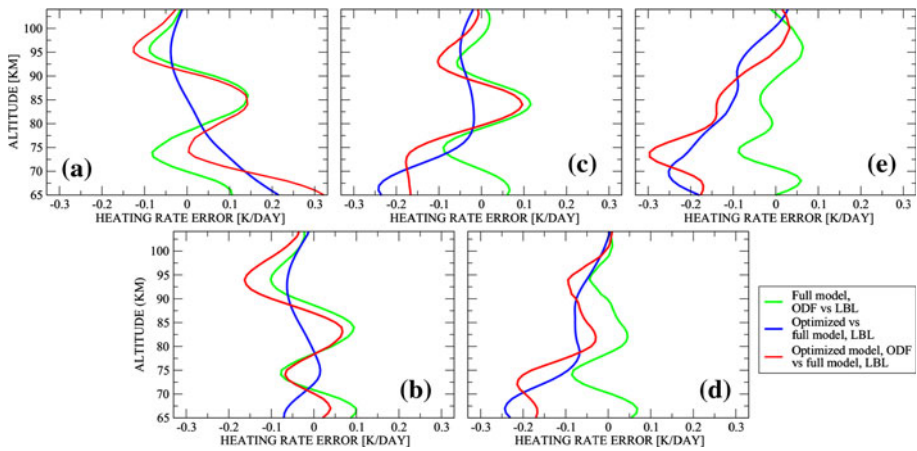
Fig. 18 Errors in CO_2 heating rates related to using an ODF in the radiative transfer calculations and an optimized set of vibrational levels. The panels correspond to the five test atmospheres: (**a**) SAW, (**b**) MLW, (**c**) TROP, (**d**) MLS, (**e**) SAS. The optimized heating rate calculation schemes are compared to the reference one (full model: 5 isotopes, 60 vibrational levels, radiative transfer calculated in line-by-line (LBL) approach). See text for ODF approach and an optimized set of levels

(3,0). For the nighttime non-LTE model of CO_2, this set reduces to 11 excited levels and "super-levels": (1,0); (2,0); (3,0); (0,1); (4,0); (1,1); (2,1) for 626 and (1,0) and (2,0) for 636 and 628. Figure 18 shows the accuracy of this approach for daytime calculations performed for five test atmospheres. In this plot, the non-LTE heating rates obtained in an optimized model are compared to that obtained for our "reference" model (5 isotopes, 60 vibrational levels). The blue lines in Fig. 18 show that the errors introduced by using an optimized model in 65–105 km interval do not exceed 0.3 K/day while the acceleration coefficient achieved is ~ 15 for daytime and ~ 25 for nighttime.

In summary, the total error associated with utilizing an optimized set of vibrational levels and applying the ODF technique for radiative transfer calculation in the molecular bands does not exceed ± 0.35 K/day for any of the test atmospheres. The method is free from any constraints on the input profiles and can provide the $h(z)$ profiles for any altitude grid. The acceleration factor of $\sim 10^3$ compared to the "reference" LBL calculations allows its utilization in modern GCMs. The same approach may be used for optimizing the $h(z)$ calculations in O_3 and H_2O. The acceleration factor for ozone will be another order of magnitude higher because of the larger number of lines in the O_3 bands.

5 Infrared Sounding of the MLT Region

In Sect. 3, we primarily considered the energetic effects of the radiation emission and absorption on the atmosphere. The emission and absorption in molecular bands can also be used to estimate the atmospheric properties like temperature, pressure, concentration of optically active atmospheric components and even the concentration of optically passive components if these components affect the populations of the rotational and vibrational states of optically active molecules. The information about these characteristics is carried by the radiation that can be registered and processed to retrieve the desired atmospheric quantities. However, the MLT is a challenging region for measurements due to a number of

reasons: (a) these heights cannot be reached by balloons or aircraft; (b) the total density and consequently the concentrations of atmospheric gases are low; (c) the vibrational, rotational, and spin levels populations start to depart from LTE thus reducing the "information content" of the radiation concerning these atmospheric layers; and (d) the temporal and spatial variability of the MLT region is high, which imposes certain criteria on the duration of the measurement. On the other hand, the high sensitivity of this region both to local and to non-local energy sources makes it a good indicator of atmospheric changes and attracts the attention of the researchers.

5.1 Atmospheric Observations in the MLT

The MLT observations can be separated into three groups: ground-based, in situ, and remote sensing from space. The measurements of the first two groups are confined to a local area while the satellite observations provide better coverage, up to global coverage. Direct ground-based sensing of the MLT region by measuring the atmospheric radiation coming to the ground is difficult because of the strong atmospheric absorption in the lower atmosphere. Lidars (for Light Detection and Ranging) overcome these difficulties by means of active sounding of the atmosphere at certain wavelengths and measuring the Rayleigh scattering, Raman scattering or fluorescence (e.g., see the overview book of Weitkamp (2005)). Using the time-resolved backscatter signal, one can retrieve the vertical distribution of the corresponding atmospheric property, such as kinetic temperature or the concentration of the trace gas. The typical accumulation time for the backscattered signal in modern lidars is on the order of tens of minutes, which is comparable to or is greater than the lifetime of the structures created by GW. Another limitation of the ground-based lidar techniques is the size of the area that can be observed (± 100 km from the lidar setup). On the other hand, lidar techniques are robust, and the retrievals do not depend on sophisticated non-LTE models that makes the lidar measurements an excellent reference dataset in the MLT. Other reference data can be obtained from the in situ measurements performed by rockets (e.g., Goldberg et al. 2004 and references therein). The atmospheric observations of this type are also limited in space and time and cannot be used for building global distributions of pressure–temperature profiles or trace gas concentrations. In this respect, the satellite-based measurements look attractive since the absorption in the upper atmospheric layers is small compared to that in the lower atmosphere, and the coverage is global. As a result, in the past two decades, satellite instruments have become the dominant source of information regarding the Earths' atmosphere in general and the MLT region in particular.

Figure 19 shows the three most common types of spaceborne observation techniques: detecting the atmospheric emissions in the limb scanning mode, registering the solar (or stellar) radiation attenuation by atmospheric absorption (the so-called occultation measurement mode), and measuring the atmospheric emissions and absorption of the terrestrial radiation in the nadir viewing mode. Compared to the other two techniques, the nadir mode is less suitable for the MLT observations. In this mode, the vertical distribution of the atmospheric properties is retrieved using the spectrally resolved radiation. The retrieval approach usually utilizes one of the modifications of Chahine's method (e.g., see Chahine 1968, 1970, 1972; Smith 1970; Barcilon 1975; Houghton et al. 1984). In this approach, a thorough selection of a set of spectral channels is needed to reduce the background radiation effects and ensure proper contributions of the layers within the altitude measurement range.
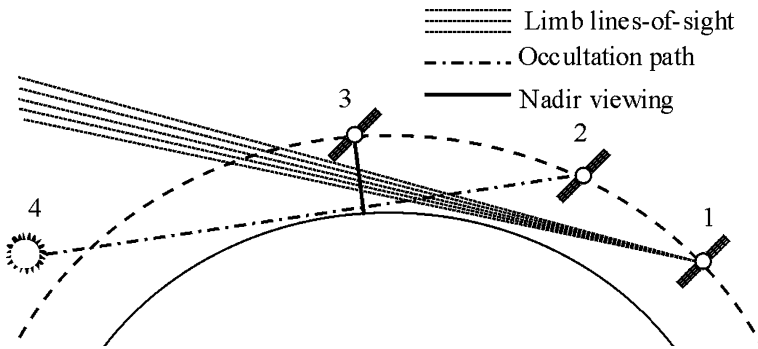
Fig. 19 Diagram illustrating atmospheric observations from space: *1*) Satellite instrument registers atmospheric emissions in the limb scanning mode; *2*) Satellite instrument registers solar radiation in occultation mode; *3*) Nadir viewing mode; *4*) Sun

In solar or stellar occultation measurements, the atmospheric parameters like density or trace gas VMRs are retrieved from the absorption profile. An obvious limitation of the occultation methods is the spatial and temporal coverage: typically the satellite instruments scan the atmosphere at sunset and sunrise once per orbit, with limited longitudinal coverage in each hemisphere. On the other hand, these methods are robust since the retrievals, in general, do not depend on the sophisticated non-LTE models: for a given molecular gas, the absorption is almost always defined by the transition from the ground state of the molecule, the concentration of which is much higher than that of other states of this molecule. The emission in the same band, which "reduces" the absorption, can be calculated in the LTE assumption for most of the cases. However, it was found that the non-LTE radiation contribution to the absorbed radiation measured by the SOFIE instrument (see Gordley et al. 2009) onboard the AIM platform (see Russell et al. 2009) is not negligible, and accounting for the non-LTE contribution in the 4.3 μm CO_2 band is needed to extend the temperature retrievals up to ~ 110 km (see Marshall et al. 2011). Overall, the solar occultation instruments like HALOE (see Russell et al. 1993), ACE-FTS (see Bernath et al. 2005) and SOFIE have demonstrated a long-term record of reliable observations that can serve as an excellent reference dataset, with far better spatio-temporal coverage than may be obtained from local measurements.

The next step toward global measurements in the upper atmosphere is to study atmospheric emissions in the limb scanning mode. In this mode, collecting the atmospheric radiation along the long limb line of sight increases the signal-to-noise ratio; pointing to space instead of pointing to the ground in the nadir observation mode removes the intense background; the vertical resolution is defined by the optical properties of the observation setup and is about 2 km for modern instruments; the spatio-temporal coverage is limited only by the orbit of the satellite. Satellite limb measurements of atmospheric thermal emissions date back to the 1970s and instruments like the Limb Radiance Inversion Radiometer (LRIR) (see Gille et al. 1980), the Stratosphere and Mesosphere Sounder (SAMS) (see Drummond et al. 1980) and the Limb Infrared Monitor of the Stratosphere (LIMS) (see Gille and Russell 1984). Later on, the altitude range for this type of measurements was extended, and the infrared emissions affected by non-LTE were observed by the Cryogenic Limb Array Etalon Spectrometer (CLAES) (see Roche et al. 1993), the Improved Stratosphere and Mesosphere Sounder (ISAMS) (see Taylor et al. 1993), and the

Michelson Interferometer for Passive Atmospheric Sounding (MIPAS) (see Fischer et al. 2008), the CRISTA, and the SABER.

Figure 20 shows an example of atmospheric limb emissions measured by the SABER radiometers for daytime and nighttime conditions. The interpretation of these measurements requires the use of a corresponding non-LTE model and an inversion algorithm. Following the general formalism (see, e.g., Rodgers 2000), the relationship between the observed radiation profile $\vec{I}$ and the state vector $\vec{X}$, which is the concentration, temperature or the VMR of the atmospheric constituent, can be described as:

$$\vec{I} = \vec{F}(\vec{X}) + \Delta\vec{I}, \tag{39}$$

where $\vec{F}(\vec{X})$ is a nonlinear functional, which represents the forward radiance calculations in limb geometry and which includes known vertical distributions of atmospheric components and non-LTE model parameters, and $\Delta\vec{I}$ is measurement error. We refer the reader to Rodgers (2000) for the review of inverse methods for atmospheric sounding. Here we consider the problem (39) in application to the MLT infrared measurements in limb geometry. The inversion of (39) in this case may be complicated due to the following reasons: (a) if the radiation at given tangent height depends on the radiation coming from other atmospheric layers, which is typical for the non-LTE conditions, the "information content" of the tangent point is reduced; (b) if the observed molecular band is optically thick, then the observed radiation remains constant or even decreases with decreasing tangent height, and the problem becomes ill-conditioned; (c) the response of limb radiation to a change in state vector (for example, an increase of temperature) can be positive (higher local temperature leads to higher population of the emitting levels) or negative (for hot bands, an increase in population of the lower level associated with higher temperature means an increase of the absorption).

Several research groups have developed retrieval algorithms for the infrared MLT observations: see, for example, Rinsland et al. (1992) for temperature, CO_2, and CO retrieval from ATMOS observations, López-Valverde et al. (1996) for CO retrieval from ISAMS measurements, Zaragoza et al. (2000) for the global distribution of CO_2 in the upper mesosphere from UARS/ISAMS observations, Mertens et al. (2001) and Gusev et al. (2006) for temperature retrievals from the SABER and CRISTA measurements, respectively, Kaufmann et al. (2002) for CO_2 and Grossmann et al. (2006) for CO retrieval from CRISTA measured spectra, Kaufmann et al. (2003) and Gil-López et al. (2005) for O_3 retrieval, Funke et al. (2009) for CO retrieval, Bermejo-Pantaleón et al. (2011) for temperature and NO, and García-Comas et al. (2011) for temperature retrievals in the MLT from MIPAS spectra, Mlynczak et al. (2007) for O_3 retrieval and Feofilov et al. (2009) for H_2O retrieval from the SABER, and Funke et al. (2005) for NO and NO_2 retrieval from the MIPAS measurements.

The majority of retrieval techniques applied for limb observations are based on the so-called "onion peeling" approach. This utilizes the specifics of limb geometry, namely that (neglecting aerosol scattering) atmospheric layers lying below the tangent height do not contribute to the measured signal. In this case, one only needs to solve a set of triangular matrices in order to get corrections to the chosen set of parameters. However, since in many cases, the tangent points are not observable (see case b) above), the rows of these matrices become linearly dependent, and the entire process collapses. In order to avoid this situation, various regularizations as well as a priori information are required to search for the so-called "physical solution", which is one of pre-calculated solutions predicting the outgoing radiation within the accuracy of measurements. The search for such a solution is
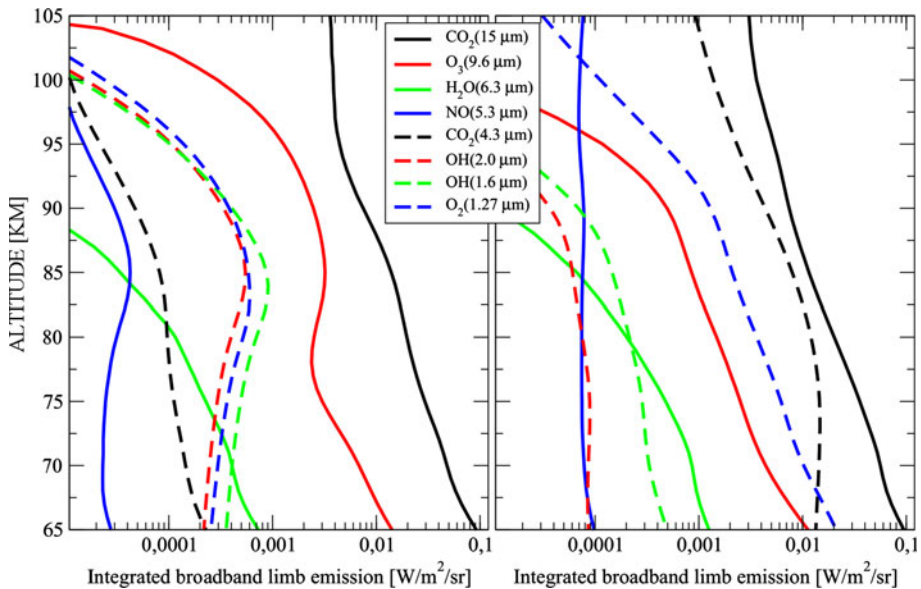
Fig. 20 Example of the SABER/TIMED limb emissions for the tropical atmosphere (2008, day 198, lat = 0 ± 5°). *Left panel* nighttime measurements ($\theta_z > 120°$ to exclude the effects of partial illumination of the upper atmosphere); *right panel* daytime measurements ($\theta_z < 85°$ to exclude twilight conditions)

usually organized as an iterative process. If the problem is nonlinear, then it is linearized, and the iterative search for the solution includes a latent iterative solution of the nonlinear problem, which often leads to time-consuming calculations and instabilities.

These complications stimulate the replacement of this inversion technique by more stable and reliable iterative forward-fit algorithm, in which the retrieval is performed iteratively. This approach avoids matrix inversion and relies on the stable and fast forward radiation calculations, a technique similar to the method described in Gordley and Russell (1981). Another advantage of the forward-fitting algorithm is that it allows straightforward accounting for the non-LTE conditions. The process starts with an initial guess for the $\vec{X}$ profile assuming that the remaining atmospheric parameters are known and fixed. The non-LTE populations are calculated and used for the limb radiation calculations. The resulting simulated radiation vector $\vec{I}_{calc}$ is compared to the measured radiation $\vec{I}_{meas}$ at each tangent height, and $\vec{X}$ is iterated using the following relaxation scheme:

$$\vec{X}^{i+1} = \vec{X}^i + (\vec{I}_{meas} - \vec{I}_{calc}^i) \cdot W, \tag{40}$$

where i and $i + 1$ denote two subsequent iterations and W is a diagonal matrix, elements of which are inversely proportional to numerically calculated derivatives of the radiation produced by the forward model with respect to $\vec{X}$ (see case c) above). After the $\vec{X}^{i+1}$ vector is updated, it is used to calculate new non-LTE populations, and the radiation is simulated again. The iterations are repeated until the differences between the simulated and measured radiation become equal to the radiation noise for a given instrument. The computational cost of this method is higher than that of a standard inversion procedure. The approximate deceleration coefficient is roughly equal to the number of iterations (7–10 depending on the radiation noise and the molecule). However, the forward-fitting algorithms demonstrate

stable convergence and are less prone to false solutions (see Rezac et al. 2011 for recent findings on the convergence of relaxation type retrieval algorithms).

This method has been successfully applied by Gusev et al. (2006) to the non-LTE temperature retrievals in the Earths MLT from the CRISTA 15 μm spectral limb radiances, by Feofilov et al. (2009) to the H_2O retrievals and Rezac (2011) to the CO_2 retrievals from the SABER radiation measurements, as well as to the temperature retrievals in the Martian atmosphere from the MGS-TES observations (see Feofilov et al. 2012b).

5.2 Peculiarities of the Atmospheric Properties Retrievals from the Non-LTE Infrared Radiation Measurements

In this section, we demonstrate two examples of the non-LTE retrievals from the infrared radiation observations in the MLT. These retrievals are single-channel retrievals that are not complicated by the cross-correlation of the two or more channels (e.g., see Rezac 2011). Still, they show the complexity of the problem and the importance of the proper modeling of all the sinks and sources for the populations of the levels responsible for the radiation formation.

5.2.1 Importance of the v_2-Quanta V–V Exchange Between the CO_2 Isotopes for Temperature Retrievals from 15 μm Radiation

For this example, we refer to Figs. 3, 7 and 8e of this work. It has been noticed that the retrieved SABER V1.06 temperatures for the polar summer mesospheric conditions (red curve in Fig. 5) differed significantly from those obtained from coincident falling sphere (FS) measurements taken during the 1–5 July 2002 summer MaCWAVE (for Mountain and Convective Waves Ascending VErtically) campaign (see Goldberg et al. 2004) and from the climatological profiles presented by Lübken (1999) for early July (compare the black, red, and green curves in Fig. 21b). Further evidence of a temperature discrepancy was obtained from the comparison of these temperatures with lidar data (e.g., see She et al. 2002; Fritts et al. 2004). One has to note that the polar summer temperature profile provides an excellent test bed for non-LTE codes due to a large difference between the mesopause and stratopause temperatures that may reach 150–180 K. Kutepov et al. (2006) have found that the discrepancy between the SABER V1.06 temperature retrievals and other measurements was caused by neglecting the V–V v_2-quanta exchange

$$CO_2^i(01101) + CO_2^j(0) \leftrightarrow CO_2^i(0) + CO_2^j(01101) \tag{41}$$

between the $CO_2(v_2)$ isotopic levels in the SABER V1.06 operational model, where i and j denote different isotopes. One has to note that the abundances of the CO_2 isotopes in the Earth's atmosphere are 0.98 for 626, 1.1×10^{-2} for 636, 3.9×10^{-3} for 628, 7.3×10^{-4} for 627, and 4.4×10^{-5} for 638 isotope. The low abundance of minor isotopes makes their spectral lines optically thin, which is crucial for the problem under consideration. In the summer polar atmosphere, the upwelling radiation from the warm stratosphere is absorbed by CO_2 molecules of minor isotopes in and around the very cold mesopause, making T_{vib} of the 01101 minor isotopic levels there significantly warmer than the kinetic temperature. This is, however, not true for the 01101 level of main isotope 626: the fundamental 15 μm band of this isotope is optically thick—allowing the exchange of radiation only between the adjacent altitude levels and keeping this T_{vib} much closer to the kinetic temperature (see Sect. 2.2).
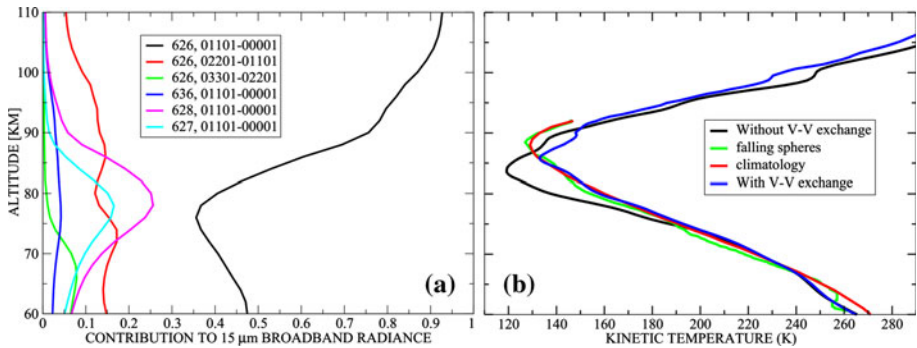
Fig. 21 The effects of ν_2-quanta V–V exchange between CO_2 isotopes on temperature retrievals from 15 μm broadband radiation (Kutepov et al. 2006) for the polar summer MLT: (**a**) contributions to broadband 15 μm limb radiation measured by SABER radiometer; (**b**) an individual temperature profile retrieved from the SABER measurements under different assumptions is compared to the collocated falling spheres measurement (Goldberg et al. 2004) and to climatology (Lübken 1999)

The radiative energy transferred to the mesopause in the optically thin isotopic bands populates the 01101 isotopic levels, which can radiate the 15 μm quanta, lose it in the collision with atomic oxygen or in the process of V–V energy transfer to the 01101 levels of the main isotope. The contributions of different isotopes to the 15 μm broadband limb radiation measured by the radiometer are shown in Fig. 21a. If the isotopic V–V exchange is not included in the model (it can be done for the convergence process acceleration, which is linked with the treatment of strongly coupled levels, see also Sect. 4.1), the isotopic 01101 levels become overpopulated and "produce" stronger 15 μm radiation in the model. Since the local temperature still has an effect on the populations of these levels (although weaker than in the LTE case), the retrieval algorithm decreases the local temperature to compensate for the increased radiation. The hydrostatic adjustment of pressure distribution in accordance with the new temperature profile moves the mesopause level downward. After the V–V exchange between CO_2 isotopes was implemented into the SABER non-LTE operational model, significant reductions of the differences between the SABER retrievals and other measurements were observed (compare the blue and magenta curves with the green and red curves in Fig. 21b). This effect is noticeable at latitudes higher than 40° in both hemispheres in the summer period (June–August in the Northern hemisphere and December-February in the Southern hemisphere).

5.2.2 V–V Coupling of $H_2O(010)$ with $O_2(1)$ and the Effects of $O_2(1)$ Level Pumping

In Sect. 3.3, we considered a model of O_2/O_3 photolysis products and its coupling with the system of H_2O vibrational levels (Fig. 14) through the V–V exchange process:

$$O_2(X^3\Sigma^-, v = 1) + H_2O(v_2) \leftrightarrow O_2(X^3\Sigma^-, v = 0) + H_2O(v_2 + 1). \qquad (42)$$
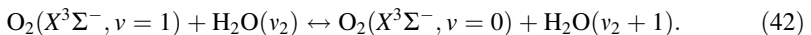
The importance of the V–V coupling of $H_2O(v_2)$ with O_2 ($X^3\Sigma^-$, v = 1) or, for simplicity, $O_2(1)$ level for correct estimating the $H_2O(010)$ level population and, therefore, for an adequate retrieval of the H_2O VMR from the 6.3 μm radiation is well known (see Sect. 3.4).

Figure 22a shows the sensitivity of the $H_2O(010)$ population to the process (42) estimated for four test atmospheric scenarios (see Yankovsky et al. 2011). The most prominent

influence of processes (42) on the population of 010 is connected with the deactivation of vibrational levels 010, 020, 030, 110, 011, 040, 120 and 021 at near-resonance V–V energy exchange with $O_2(1)$ above 70 km, which leads to a significant decrease of the 010 level population at 80–85 km, in comparison with the population of the $H_2O(010)$ calculated without taking this process into account. Since the H_2O and O_2 systems are coupled, the next step is to include the pumping of $O_2(1)$ level through a set of processes shown in the upper panel of Fig. 14 and described in detail in Yankovsky and Manuilova (2006). However, including all these processes into the operational retrieval algorithm is too complicated and computationally expensive. Instead, the approximate quantum yield ε for $O_2(1)$ molecules production per one act of O_3 photolysis is used (e.g., see López-Puertas and Taylor 2001). In this approach, the value of quantum yield is equal to 4 and does not change with altitude. Recently, Yankovsky et al. (2011) used the model of Yankovsky and Manuilova (2006) and studied the behavior of the quantum yield ε with respect to latitude, season, solar zenith angle, and O_3 photolysis in the Hartley, Huggins, Chappuis and Wulf bands (200–900 nm). They found that ε depends weakly on latitude, season, and solar zenith angle, and they suggested a simple parameterization formula for the altitude dependence of this parameter:

$$\varepsilon = e^{a + b(\ln(P))^2 + c \cdot P}, \tag{43}$$

where $a = 2.1370 \pm 0.0328$, $b = -0.0366 \pm 0.00207$, and $c = -0.1099 \pm 0.0720$ are the parameterization coefficients, and P is pressure in hPa.

The comparisons of variable ε versus fixed $\varepsilon = 4$ calculations are shown in Fig. 22b. The behavior of the $H_2O(010)$ in this figure requires some comment. The 3–5 % increase in $H_2O(010)$ population at 60–70 km altitude is due to an increased pumping from $O_2(1)$ since ε is greater than 4 here. However, the region above 80 km altitude also experiences an increase in $H_2O(010)$ population even though ε is less than 4 at these heights. This is explained by the non-local nature of radiation in the MLT region: the $H_2O(010)$ levels in the mesopause are sensitive to radiation coming from other parts of the atmosphere. Increased quantum yield at 60–70 km altitudes leads to stronger pumping of the $H_2O(010)$ levels and, therefore, to an increase in 6.3 μm radiation coming up to the mesopause region. Correspondingly, this increased radiation leads to stronger excitation of the $H_2O(010)$ levels in the mesopause region. Neglecting the variability of ε will lead to an overestimate of the retrieved H_2O VMR in the MLT area by at least 5 %. The approach described has been incorporated into the H_2O non-LTE model in the SABER operational code and will be used for H_2O VMR retrievals in the next release of the SABER data.

6 Summary

This paper discusses the formation mechanisms of infrared radiation and its interaction with the matter in the mesosphere and lower thermosphere. A distinctive feature of this region is the breakdown of local thermodynamic equilibrium for the vibrational levels of the molecules involved in these mechanisms. Therefore, we concentrate mainly on the discussing the non-LTE models of IR radiation formation as well as on the methodology of the non-LTE problem solution with an aim to overview the current status of this methodology and corresponding applications for the energy budget calculations and interpretation of space observations, and indicate important, to our mind, directions of further activities.
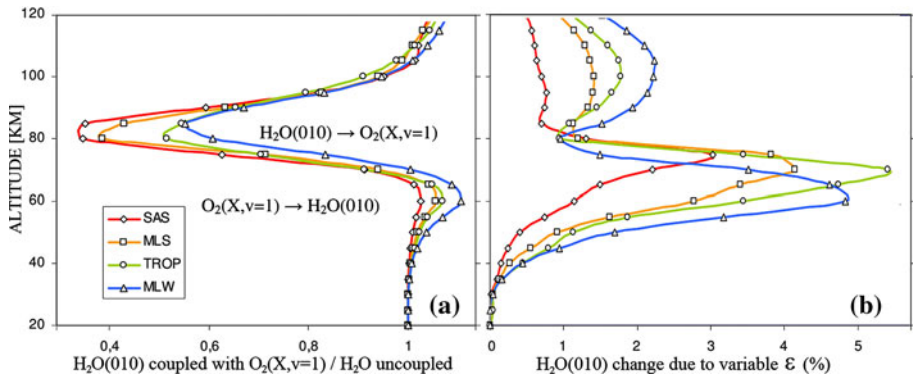
Fig. 22 Tests (Yankovsky et al. 2011) showing the importance of correctly accounting for the V–V exchanges with $O_2(X, v = 1)$ in the H_2O non-LTE model: (**a**) sensitivity of $H_2O(010)$ level population to $H_2O(010)$–$O_2(X, v = 1)$ coupling for four test atmospheric scenarios; (**b**) sensitivity of $H_2O(010)$ level population to the efficiency of $O_2(X, v = 1)$ level pumping from the O_2/O_3 photolysis products (Sect. 3.3); the $H_2O(010)$ populations computed with variable quantum yield ε are compared with the $H_2O(010)$ populations estimated with $\varepsilon = 4$ (see text)

The non-LTE models for three most important (for the MLT energy budget) molecules CO_2, O_3, and H_2O are described in detail, and the contributions of these molecules to the radiative energy budget are estimated for five test atmospheres, ranging from polar winter to polar summer. As it was shown in a number of studies, CO_2 is the main cooler of the MLT: the cooling increases with increasing altitude up to about 110–130 km (depending on the atmospheric model) reaching maxima of the order of tens of K/day. The LTE breakdown for $CO_2(v_2)$ levels occurs at altitudes above ~ 85 km and the magnitude of the cooling strongly depends on the $CO_2(v_2)-O$ quenching rate coefficient. However, there is an unresolved discrepancy between the laboratory measurements and atmospheric retrievals of this rate coefficient. We address this problem and describe recent attempt to estimate this coefficient from atmospheric measurements, which obviously indicates the need for further theoretical and experimental studies of this collisional process.

For O_3, the net effect is cooling at altitudes below ~ 70 km and heating above ~ 75 km, which reaches 2–3 K/day at ~ 90–95 km altitude. The combined effect of the rotational and vibrational H_2O bands in the MLT region is a cooling of ~ 1.0–1.5 K/day at ~ 75 km; this cooling decreases with increasing altitude. We also address a new term of the energy budget, namely, the additional radiative cooling caused by fluctuations of the atmospheric vertical structure induced by small-scale (sub-grid) gravity waves, which are poorly resolved in the current GCMs and show that it can reach ~ 4 K/day at the mesopause altitude.

Another problem addressed in this paper is the efficiency and accuracy of the IR radiative heating rate estimations. The radiative heating rates in modern GCMs are usually parameterized. A number of efficient parameterization schemes have been developed up to now, which, however, have limited accuracy and flexibility. In this paper, we propose a way for optimizing exact algorithms of the non-LTE heating rate calculations for further usage in GCMs aimed at keeping the accuracy and flexibility of LBL calculations. Three key steps of this optimization are (a) utilizing accelerated lambda iterations (ALI) as the most advanced technique for solving the non-LTE problem, (b) using the opacity distribution function (ODF) approach for treating the branches of molecular bands as single

spectral "super-lines", and (c) reducing the number of vibrational levels. As we show, these three features ensure an efficient and flexible calculation algorithm with controlled accuracy that can be used in modern GCMs as a replacement for parameterizations.

Another important aspect addressed in the paper is the quality of non-LTE models applied for the interpretation of the infrared emissions observations of the MLT region. These models require precise and detailed accounting for all known mechanism of molecular vibration excitation, exchange and quenching. To illustrate that, we use the SABER infrared limb observations in the 15 µm and 6.3 µm channels and the corresponding $T(z)$ and $H_2O(z)$ retrievals. We show that omission of the process of V–V v_2 quanta exchange between the main and "minor" CO_2 isotopes ($\sim 1.5\ \%$ in abundance in total) leads to a ~ 10 K underestimate of the mesopause temperature for polar summer conditions. We also demonstrate how simplification of the $O_2(1)$ level pumping in the O_2/O_3 photolysis products kinetics scheme leads to an underestimate of the 6.3 µm H_2O radiation between 50 and 70 km altitude and, correspondingly, to 5–10 % overestimate of H_2O VMR retrieved from 6.3 µm radiation measured in this region.

References

Allen DC, Scragg T, Simpson CJSM (1980) Low temperature fluorescence studies of the deactivation of the bend-stretch manifold of CO_2. Chem Phys 51:279–298

Anderson LS (1987) An algorithm for the simultaneous solution of thousands of transfer equations under global constraints. In: Kalkofen W (ed) Numerical radiative transfer. Cambridge University Press, Cambridge, pp 163–190

Balakrishnan N, Kharchenko V, Dalgarno A (1998) Slowing of energetic $O(^3P)$ atoms in collisions with N_2. J Geophys Res 103:23393–23398

Barcilon TV (1975) On Chahine's relaxation method for the radiative transfer equation. J Atmos Sci 32:1626–1630

Bermejo-Pantaleón D, Funke B, López-Puertas M, García-Comas M, Stiller G, von Clarmann T, Linden A, Grabowski U, Höpfner M, Kiefer M, Glatthor N, Kellmann S, Lu G (2011) Global observations of thermospheric temperature and nitric oxide from MIPAS spectra at 5.3 µm. J Geophys Res 116(A10):A10313

Bernath PF, McElroy CT, Abrams MC, Boone CD, Butler M, Camy-Peyret C, Carleer M, Clerbaux C, Coheur PF, Colin R, DeCola P, DeMazière M, Drummond JR, Dufour D, Evans WFJ, Fast H, Fussen D, Gilbert K, Jennings DE, Llewellyn EJ, Lowe RP, Mahieu E, McConnell JC, McHugh M, McLeod SD, Michaud R, Midwinter C, Nassar R, Nichitiu F, Nowlan C, Rinsland CP, Rochon YJ, Rowlands N, Semeniuk K, Simon P, Skelton R, Sloan JJ, Soucy MA, Strong K, Tremblay P, Turnbull D, Walker KA, Walkty I, Wardle DA, Wehrle V, Zander R, Zou J (2005) Atmospheric chemistry experiment (ACE): mission overview. Geophys Res Lett 32:L15S01. doi:10.1029/2005GL022386

Bougher SW, Hunten DM, Roble RG (1994) CO_2 cooling in terrestrial planet thermospheres. J Geophys Res 99:14609–14622

Brasseur GP, Solomon S (2005) Aeronomy of the middle atmosphere. Springer, New York

Brion J, Chakir A, Charbonnier J, Daumont D, Parisse C, Malicet J (1998) Absorption spectra measurements for the ozone molecule in the 350–830 nm region. J Atm Chem 30:291–299

Castle KJ, Kleissas KM, Rhinehart JM, Hwang ES, Dodd JA (2006) Vibrational relaxation of $CO_2(v_2)$ by atomic oxygen. J Geophys Res 111(A09303). doi:10.1029/2006JA011736

Castle KJ, Black LA, Simione MW, Dodd JA (2012) Vibrational relaxation of $CO_2(v_2)$ by $O(^3P)$ in the 142–490 K temperature range. J Geophys Res. doi:10.1029/2012JA017519

Center RE (1973) Vibrational relaxation of CO_2 by O atoms. J Chem Phys 59(7):3523–3528

Chabrillat S, Kockarts G (1997) Simple parameterization of the absorption of the solar Lyman-α line. Geophys Res Lett 24:2659–2662

Chahine MT (1968) Determination of the temperature profile in an atmosphere from its outgoing radiance. J Opt Soc Am 58:1634–1637

Chahine MT (1970) Inverse problems in radiative transfer: determination of atmospheric parameters. J Atmos Sci 27:960–967

Chahine MT (1972) A general relaxation method for inverse solution of the full radiative transfer equation. J Atmos Sci 29:741–747

Crutzen PJ (1970) Discussion of paper "Absorption and emission by carbon dioxide in the atmosphere" by JT Houghton. Quart J R Met Soc 96:767–770

DeMajistre R, Yee JH, Zhu X (2001) Parameterizations of oxygen photolysis and energy deposition rates due to solar energy absorption in the Schumann-Runge continuum. Geophys Res Lett 28(16):3163–3166

DeMore WB, Golden DM, Hampson RF, Howard CJ, Kolb CE, Molina MJ (1997) Chemical kinetics and photo-chemical data for use in stratospheric modeling. JPL Publ 97–4:1–128

Dickinson RE (1984) Infrared radiative cooling in the mesosphere and lower thermosphere. J Atmos Sol Terr Phys 46:995–1008

Drummond JR, Houghton JT, Peskett GD, Rodgers CD, Wale MJ, Whitney J, Williamson EJ (1980) The stratospheric and mesospheric sounder on nimbus 7. Philos Trans R Soc Lond A296:219–241

Feofilov AG, Kutepov AA, Medvedev AS, Hartogh P (2006) New technique for calculating the non-LTE infrared radiative cooling/heating rates in the Martian GCM. In: Forget F, López-Valverde MA, Desjean MC, Huot JP, Lefevre F, Lebonnois S, Lewis SR, Millour E, Read PL, Wilson RJ (eds) Second workshop on Mars atmosphere modelling and observations, held February 27–March 3, 2006. LMD, IAA, AOPP, CNES, ESA, Granada, Spain, pp 614–617

Feofilov AG, Kutepov AA, Pesnell WD, Goldberg RA, Marshall BT, Gordley LL, García-Comas M, López-Puertas M, Manuilova RO, Yankovsky VA, Petelina SV, Russell JM III (2009) Daytime SABER/TIMED observations of water vapor in the mesosphere: retrieval approach and first results. Atmos Chem Phys 9:8139–8158

Feofilov AG, Kutepov AA, She C-Y, Smith AK, Pesnell WD, Goldberg RA (2012a) $CO_2(v_2)$-O quenching rate coefficient derived from coincidental SABER/TIMED and Fort Collins lidar observations of the mesosphere and lower thermosphere. Atmos Chem Phys 12:9013–9023. doi:10.5194/acp-12-9013-2012

Feofilov AG, Kutepov AA, Rezac L, Smith MD (2012b) Extending MGS-TES temperature retrievals in the Martian atmosphere up to 90 km: retrieval approach and results. Icarus 221:949–959. doi:10.1016/j.icarus.2012.09.033

Fernandez RP, Kaufmann M, Toselli BM (2009) Relative importance of ozone energy transfer processes in the middle atmosphere. J Atmos Sol Terr Phys 71:805–815

Fernandez RP, Kaufmann M, Toselli BM (2010) Effects of the inclusion of bending-to-stretching transitions in the non-LTE modeling of ozone vibrational temperatures. J Atmos Sol Terr Phys 72:890–899

Fischer H, Birk M, Blom C, Carli B, Carlotti M, von Clarmann T, Delbouille L, Dudhia A, Ehhalt D, Endemann M, Flaud JM, Gessner R, Kleinert A, Koopman R, Langen J, López-Puertas M, Mosner P, Nett H, Oelhaf H, Perron G, Remedios J, Ridolfi M, Stiller G, Zander R (2008) MIPAS: an instrument for atmospheric and climate research. Atmos Chem Phys 8:2151–2188

Fomichev VI (2009) The radiative energy budget of the middle atmosphere and its parameterization in general circulation models. J Atmos Sol Terr Phys 71:1577–1585

Fomichev VI, Kutepov AA, Akmaev RA, Shved GM (1993) Parameterization of the 15 μm CO_2 band cooling in the middle atmosphere (15–115 km). J Atmos Terr Phys 55:7

Fomichev VI, Blanchet J-P, Turner DS (1998) Matrix parameterization of the 15 μm CO_2 band cooling in the middle and upper atmosphere for variable CO_2 concentration. J Geophys Res 103(D10):11505–11528

Fomichev VI, Ogibalov VP, Beagley SR (2004) Solar heating by the near-IR CO_2 bands in the mesosphere. Geophys Res Lett 31:L21102

Frisch U, Frisch H (1975) Non-LTE transfer, $\sqrt{\varepsilon}$ revised. Mon Not R Astron Soc 173:167–182

Fritts DC, Alexander MJ (2003) Gravity wave dynamics and effects in the middle atmosphere. Rev Geophys 41(1):1003–1067. doi:10.1029/2001RG000106

Fritts DC, Williams BP, She C-Y, Vance JD, Rapp M, Lübken F-J, Müllemann A, Schmidlin FJ, Goldberg RA (2004) Observations of extreme temperature and wind gradients near the summer mesopause during the MaCWAVE/MIDAS rocket campaign. Geophys Res Lett 31:L24S06. doi:10.1029/2003GL019389

Fu K, Liou KN (1992) On the correlated k-distribution method for radiative transfer in nonhomogeneous atmospheres. J Atmos Sci 49:2139–2156

Funke B, López-Puertas M, von Clarmann T, Stiller GP, Fischer H, Glatthor N, Grabowski U, Höpfner M, Kellmann S, Kiefer M, Linden A, Mengistu Tsidu G, Milz M, Steck T, Wang DY (2005) Retrieval of stratospheric NOx from 5.3 and 6.2 μm nonlocal thermodynamic equilibrium emissions measured by Michelson Interferometer for Passive Atmospheric Sounding (MIPAS) on Envisat. J Geophys Res 110:D09302. doi:10.1029/2004JD005

Funke B, López-Puertas M, García-Comas M, Stiller G, von Clarmann T, Höpfner M, Glatthor N, Grabowski U, Kellmann S, Linden A (2009) Carbon monoxide distributions from the upper troposphere to the mesosphere inferred from 4.7 μm non-local thermal equilibrium emissions measured by MIPAS on Envisat. Atmos. Chem Phys 9(7):2387–2411

Funke B, López-Puertas M, García-Comas M, Kaufmann M, Höpfner M, Stiller GP (2012) GRANADA: a generic radiative transfer and non-LTE population algorithm. J Quant Spectrosc Radiat Transf 113(14):1771–1817

Garcia RR, Solomon S (1994) A new numerical model of the middle atmosphere. 2. Ozone and related species. J Geophys Res 99(D6):12937–12951

García-Comas M, López-Puertas M, Mertens CJ, Mlynczak MG, Russell JM III, Remsberg EE, Gordley LL, Kalogerakis KS, Copeland RA, Slanger TG (2002) The role of the quenching of $O_2(1)$ by atomic oxygen on 6.3 μm atmospheric radiances and its impact on the retrieval of water vapour. AGU Fall Meet Abstr A512+

García-Comas M, Funke B, López-Puertas M, Bermejo-Pantaleón D, Glatthor N, von Clarmann T, Stiller G, Grabowski U, Boone CD, French WJR, Leblanc T, López-González MJ, Schwartz MJ (2011) On the quality of MIPAS kinetic temperature in the middle atmosphere. Atmos Chem Phys Discuss 11(8):24233–24312

Gille JC, Russell JM III (1984) The limb infrared monitor of the stratosphere—experiment description, performance, and results. J Geophys Res 89(D4):5125–5140

Gille JC, Bailey PL, Russell JM III (1980) Temperature and composition measurements from the LRIR and LIMS experiments on Nimbus 6 and 7. Philos Trans R Soc A 89:205–218

Gil-López S, López-Puertas M, Kaufmann M, Funke B, García-Comas M, Koukouli ME, Glatthor N, Grabowski U, Höpfner M, Stiller GP, von Clarmann T (2005) Retrieval of stratospheric and mesospheric O_3 from high resolution MIPAS spectra at 15 and 10 μm. Adv Sp Res 36(5):943–951

Goldberg RA, Fritts DC, Williams BP, Lübken F-J, Rapp M, Singer W, Latteck R, Hoffmann P, Mullemann A, Baumgarten G, Schmidlin FJ, She C-Y, Krueger DA (2004) The MaCWAVE/MIDAS rocket and ground-based measurements of polar summer dynamics: overview and mean state structure. Geophys Res Lett 31:L24S02. doi:10.1029/2004GL019411

Goody RM, Yung YL (1995) Atmospheric radiation: theoretical basis. Oxford University Press, USA

Goody RM, West R, Chen L, Crisp D (1989) The correlated-k method for radiation calculations in non-homogeneous atmospheres. J Quant Spectr Rad Trans 42:539–550

Gordiets BF (1976) A model of the upper atmosphere radiating in infrared spectrum. Kratkie Soobsch Fiz 6:40

Gordiets BF, Kulikov YuN, Markov MN, Marov MYa (1982) Numerical modelling of the thermospheric heat budget. J Geophys Res 87(A6):4504–4514

Gordley LL, Russell JM III (1981) Rapid inversion of limb radiance using an emissivity growth approximation. Appl Opt 20:807–813

Gordley LL, Hervig M, Fish C, Russell JM III, Cook J, Hanson S, Shumway A, Bailey S, Paxton G, Deaver L, Marshall BT, Burton J, Magill B, Brown C, Thompson E, Kemp J (2009) The solar occultation for ice experiment (SOFIE). J Atmos Sol Terr Phys 71:285–299. doi:10.1016/JjastP2008.07.012

Grossmann KU, Offermann D, Gusev O, Oberheide J, Riese M, Spang R (2002) The CRISTA-2 mission. J Geophys Res 107(D23):8173–8185. doi:10.1029/2001JD000667

Grossmann KU, Gusev O, Knieling P (2006) The distribution of carbon monoxide in the upper mesosphere and lower thermosphere during CRISTA-1 and CRISTA-2. J Atm Sol Terr Phys 68(15):1764–1780. doi:10.1016/JjastP2006.05.022

Gusev OA (2003) Non-LTE diagnostics of infrared observations of the planetary atmospheres. PhD thesis. University of Munich, http://deposiTddBde/cgi-bin/dokserv?idn=968893651&dok_var = d1&dok_ext = pdf&filename = 968893651.pdf

Gusev OA, Kutepov AA (2003) Non-LTE gas in planetary atmospheres. In: Hubeny I, Mihalas D, Werner K (eds) Stellar atmosphere modeling, ASP conference series, vol 288, pp 318–330

Gusev O, Kaufmann M, Grossmann KU, Schmidlin FJ, Shepherd MG (2006) Atmospheric neutral temperature distribution at the mesopause/turbopause altitude. J Atmos Sol Terr Phys 68(15):1684–1697. doi:10.1016/JjastP2005.12.010

Harris RD, Adams GW (1983) Where does the O(1D) energy go? J Geophys Res 88(A6):4918–4928

Hartogh P, Medvedev AS, Kuroda T, Saito R, Feofilov AG, Kutepov AA, Berger U (2005) Description and climatology of a new general circulation model of the Martian atmosphere. J Geophys Res 110:E11008. doi:10.1029/2005JE002498

Houghton JT, Taylor FW, Rodgers CD (1984 republished 2009) Remote soundings of atmospheres, Cambridge University Press, Cambridge, New York, Series title: Cambridge planetary science series, 343 pp

Hubeny I, Lanz T (2003) Model photospheres with accelerated lambda iteration. In: Hubeny I, Mihalas D, Werner K (eds) Stellar atmosphere modeling, ASP conference series, vol 288, pp 51–68

Hubeny I, Mihalas D, Werner K (eds) (2003) Stellar atmosphere modeling, ASP Conference Series, vol 288, 697 pp

Huestis DL (2006) Vibrational energy transfer and relaxation in O_2 and H_2O. J Phys Chem A 110:6638–6642

Huestis DL, Bougher SW, Fox JL, Galand M, Johnson RE, Moses JI, Pickering JC (2008) Cross sections and reaction rates for comparative planetary aeronomy. Space Sci Rev 139:63–105. doi:10.1007/s11214-008-9383-7

Ivanov VV (1973) Transfer of radiation in spectral lines. National Bureau of Standards Special Publication N385, US Government Printing Office, Washington, DC

Kaufmann M, Gusev OA, Grossmann KU, Roble RG, Hagan ME, Hartsough C, Kutepov AA (2002) The vertical and horizontal distribution of CO_2 densities in the upper mesosphere and lower thermosphere as measured by CRISTA. J Geophys Res D107:8182–8200. doi:10.1029/2001JD000704

Kaufmann M, Gusev OA, Grossmann KU, Martin-Torres FJ, Marsh DR, Kutepov AA (2003) Satellite observations of daytime and nighttime ozone in the mesosphere and lower thermosphere. J Geophys Res 108(D9):4272–4285. doi:10.1029/2002JD002800

Kaufmann M, Gil-López S, López-Puertas M, Funke B, García-Comas M, Glatthor N, Grabowski U, Höpfner M, Stiller GP, von Clarmann T, Koukouli ME, Hoffmann L, Riese M (2006) Vibrationally excited ozone in the middle atmosphere. J Atmos Sol Terr Phys 68(2):202–212

Kharchenko V, Dalgarno A, Fox JL (2005) Thermospheric distribution of fast O(^{1}D) atoms. J Geophys Res 110:A12305–A12313. doi:10.1029/2005JA011232

Khvorostovskaya LE, Potekhin IYu, Shved GM, Ogibalov VP, Uzyukova TV (2002) Measurement of the rate constant for quenching CO_2(0110) by atomic oxygen at low temperatures: reassessment of the rate of cooling by the CO_2 15-µm emission in the lower thermosphere. Izvestiya Atmos Ocean Phys 38:613–624

Kockarts G (1994) Penetration of solar radiation in the Schumann-Runge bands of moleculated oxygen: a robust approximation. Ann Geophys 12:1207–1217

Körner U, Sonnemann GR (2001) Global three-dimensional modeling of the water vapor concentration of the mesosphere-mesopause region and implications with respect to the noctilucent cloud region. J Geophys Res 106(9):9639–9651

Koukouli ME, López-Puertas M, Gil-López S, Funke B, Milz M, for the IAA/IMK MIPAS/ENVISAT team (2006) Water vapour profiles and non-LTE parameters from its mesospheric emissions derived from MIPAS/ENVISAT. In: Geophys Res Abstr 8: 03303, SRef-ID: 1607-7962/gra/EGU06-A-03303

Kumer JB, James TC (1983) SPIRE data evaluation and nuclear IR fluorescence processes, Report DNAOOI-79-C-0033. AFGL, Bedford

Kutepov AA, Fomichev VI (1993) Application of the second-order escape probability approximation to the solution of the NLTE vibration–rotation band radiative transfer problem. J Atmos Terr Phys 55:1–6

Kutepov AA, Gusev OA, Ogibalov VP (1998) Solution of the non-LTE problem for molecular gas in planetary atmospheres: superiority of accelerated lambda iteration. J Quant Spectrosc Radiat Transf 60:199–220

Kutepov AA, Feofilov AG, Marshall BT, Gordley LL, Pesnell WD, Goldberg RA, Russell JM III (2006) SABER temperature observations in the summer polar mesosphere and lower thermosphere: importance of accounting for the CO_2 v2 quanta V–V exchange. Geophys Res Lett 33:L21809–L21813. doi:10.1029/2006GL026591

Kutepov AA, Feofilov AG, Medvedev AS, Pauldrach AWA, Hartogh P (2007) Small-scale temperature fluctuations associated with gravity waves cause additional radiative cooling of the mesopause region. Geophys Res Lett 34:L24807–L24811. doi:10.1029/2007GL032392

Kutepov AA, Feofilov AG, Medvedev AS, Berger U, Kaufmann M, Pauldrach AWA (2012) Infra-red radiative cooling/heating of the mesosphere and lower thermosphere due to the small-scale temperature fluctuations associated with gravity waves. In: Lubken FJ (ed) Climate and weather of the sun-earth system (CAWSES), Springer, pp 429–442

Lacis AA, Oinas VA (1991) Description of the correlated k-distribution method for modeling nongrey gaseous absorption, thermal emission, and multiple scattering in vertically inhomogeneous atmospheres. J Geophys Res 96:9027–9063

Levine RD, Bernstein RB (1974) Energy disposal and energy consumption in elementary chemical reactions: the information theoretic approach. Acc Chem Res 7(12):393–400

Lilenfeld HV (1994) Deactivation of vibrationally-excited NO and CO_2 by O-atoms. Final technical rept, 28 Sep 89-15 Jun 94, http://handlEdtiCmil/100.2/ADA298581, ADA298581

López-Puertas M, Taylor FW (2001) Non-LTE radiative transfer in the atmosphere. World Scientific Publishing Co, River Edge

López-Puertas M, López-Valverde MA, Rinsland CP, Gunson MR (1992) Analysis of the upper atmosphere $CO_2(v_2)$ vibrational temperatures retrieved from ATMOS/Spacelab 3 observations. J Geophys Res 97(D18):20,469–20,478

López-Valverde MA, López-Puertas M, Remedios JJ, Rodgers CD, Taylor FW, Zipf EC, Erdman PW (1996) Validation of measurements of carbon monoxide from the improved stratospheric and mesospheric sounder. J Geophys Res 101(D):9929–9956. doi:10.1029/95JD01715

Lübken F-J (1999) Thermal structure of the Arctic summer mesosphere. J Geophys Res 104:9135–9149

Lübken F-J, Rapp M, Strelnikova I (2007) The sensitivity of mesospheric ice layers to atmospheric background temperatures and water vapor. Adv Space Res 40:794–801

Maguire WC, Pearl JC, Smith MD, Conrath BJ, Kutepov AA, Kaelberer MS, Winter E, Christensen PR (2002) Observation of high altitude, CO_2 hot bands on Mars by the orbiting thermal emission Spectrometer. J Geophys Res E107:5063–5067. doi:10.1029/2001JE001516

Malicet J, Daumont D, Charbonnier J, Parisse C, Chakir A, Brion J (1995) Ozone UV spectroscopy absorption cross-sections and temperature dependence. J Atmos Chem 21(4):263–273. doi:10.1007/BF00696758

Manuilova RO, Shved GM (1992) The 4.8 and 9.6 µm ozone band emissions in the middle atmosphere. J Atmos Terr Phys 54(9):1149–1168

Manuilova RO, Gusev OA, Kutepov AA, Von Clarmann T, Oelhaf H, Stiller GP, Wegner A, López-Puertas M, Martin-Torres FJ, Zaragoza Gand Flaud JM (1998) Modelling of non-LTE Limb spectra of IR ozone bands for the MIPAS space experiment. J Quant Spect Radiat Transf 59(3–5):405–422

Manuilova RO, Yankovsky VA, Semenov AO, Gusev OA, Kutepov AA, Sulakshina ON, Borkov YuG (2001) Non-equilibrium emission of the middle atmosphere in the IR ro-vibrational water vapor bands. Atmos Ocean Opt 14:864–867

Marshall BT, Deaver LE, Thompson RE, Gordley LL, McHugh MJ, Hervig ME, Russell JM III (2011) Retrieval of temperature and pressure using broadband solar occultation: SOFIE approach and results. Atmos Meas Tech 4:893–907. doi:10.5194/amt-4-893-2011

Mertens CJ, Mlynczak MG, López-Puertas M, Wintersteiner PP, Picard RH, Winick JR, Gordley LL, Russell JM III (2001) Retrieval of mesospheric and lower thermospheric kinetic temperature from measurements of CO_2 15 µm Earth limb emission under non-LTE conditions. Geophys Res Lett 28(7):1391–1394

Mihalas D (1978) Stellar atmospheres, 2nd edn. Freeman and Co, San Francisco

Minschwaner K, Anderson GP, Hall LA, Yoshino K (1992) Polynomial coefficients for calculating O_2 Schumann-Runge cross sections at 0.5 cm^{-1} resolution. J Geophys Res 97:10103–10108

Mlynczak MG, Marshall BT (1996) A reexamination of the role of solar heating in the O_2 atmospheric and infrared atmospheric bands. Geophys Res Lett 23:657–660

Mlynczak MG, Solomon S (1993) A detailed evaluation of the heating efficiency in the middle atmosphere. J Geophys Res 98:10517–10541

Mlynczak MG, Solomon SC, Zaras DS (1993) An updated model for $O_2(1\Delta_g)$ concentrations in the mesosphere and lower thermosphere and implications for remote sensing of ozone at 1.27 µm. J Geophys Res D 98:18639–18648

Mlynczak MG, Morgan F, Yee J-H, Espy P, Murtagh D, Marshall B, Schmidlin F (2001) Simultaneous measurements of the $O_2(^1\Delta)$ and $O_2(^1\Sigma)$ airglows and ozone in the daytime mesosphere. Geophys Res Lett 28(6):999–1002

Mlynczak MG, Marshall BT, Martin-Torres FJ, Russell JM III, Thompson RE, Remsberg EE, Gordley LL (2007) Sounding of the atmosphere using broadband emission radiometry observations of daytime mesospheric O_2 (1Δ) 1.27 µm emission and derivation of ozone, atomic oxygen, and solar and chemical energy deposition rates. J Geophys Res 112(D15306). doi:10.1029/2006JD008355

Nee JB, Lee PC (1997) Detection of $O(^1D)$ produced in the photodissociation of O_2 in the Schumann-Runge continuum. J Phys Chem A 101(36):6653–6657

Offermann D, Grossmann KU, Barthol P, Knieling P, Riese M, Trant R (1999) Cryogenic infrared spectrometers and telescopes for the atmosphere (CRISTA) experiment and middle atmosphere variability. J Geophys Res 104:16311–16325

Ogibalov VP (2000) The CO_2 non-LTE problem taking account of the Multiquantum transitions on the ν_2-mode during CO_2-O collisions. Phys Chem Earth (B) 25(5–6):493–499

Pauldrach AWA (2003) Hot stars: old-fashioned or trendy? Rev Modern Astron 16:133–170

Pauldrach AWA, Kudritzki RP, Puls J, Butler K, Hunsinger J (1994) Radiation driven winds of hot luminous stars—XII. A first step towards detailed UV line diagnostics of O-stars. Astron Astrophys 283:525–560

Pauldrach AWA, Hoffmann TL, Lennon M (2001) Radiation driven winds of hot luminous stars—XIII. A description of NLTE line blocking and blanketing towards realistic models for expanding atmospheres. Astron Astrophys 375:161–202. doi:10.1051/0004-6361:20021443

Petelina SV, Zasetsky AY (2009) Temperature of mesospheric ice retrieved from the O-H stretch band. Geophys Res Lett 36:L15804. doi:10.1029/2009GL038488

Pollock DS, Scott GBI, Phillips LF (1993) Rate constant for quenching of $CO_2(010)$ by atomic oxygen. Geophys Res Lett 20:727–729

Press WH, Teukolsky SA, Vetterling WT, Flannery BP (2002) Numerical recipes in C ++, the art of scientific computing, 2nd edn. Cambridge University Press, Cambridge

Rapp M, Thomas GE (2006) Modeling the microphysics of mesospheric ice particles: assessment of current capabilities and basic sensitivities. J Atmos Sol Terr Phys 68(7):715–744

Ratkowski AJ, Picard RH, Winick JR, Grossmann KU, Homann D, Ulwick JC, Paboojian AJ (1994) Lower-thermospheric infra-red emissions from minor species during high-latitude twilight—B: analysis of 15 μm emission and comparison with non-LTE models. J Atmos Terr Phys 56:1899–1914

Remsberg EE, Marshall BT, Garcia-Comas M, Krueger D, Lingenfelser GS, Martin-Torres J, Mlynczak MG, Russell JM III, Smith AK, Zhao Y, Brown C, Gordley LL, López-Gonzalez MJ, López-Puertas M, She C-Y, Taylor MJ, Thompson RE (2008) Assessment of the quality of the Version 1.07 temperature-versus-pressure profiles of the middle atmosphere from TIMED/SABER. J Geophys Res 113(D17):1–27. doi:10.1029/2008JD010013

Rezac L (2011) Simultaneous retrieval of T(p) and CO_2 volume mixing ratio from limb observations of infrared radiance under non-LTE conditions, PhD thesis, http://dl.dropbox.com/u/44230060/Ladislav-Rezac-PhD-thesis-2011.pdf, Hampton University of Virginia, 163 pp

Rezac L, Kutepov AA, Feofilov AG, Russell JM III (2011) On limb radiance calculations and convergence of relaxation type retrieval algorithms. Appl Opt 50(28):5499–5502

Rinsland C, Gunson MR, Zander R, López-Puertas M (1992) Middle and upper atmosphere pressure-temperature profiles and the abundances of CO_2 and CO in the upper atmosphere from ATMOS/Spacelab 3 observations. J Geophys Res 97:20479

Roche AE, Kumer JB, Merganthaler JL, Ely GA, Ulpinger WG, Potter JF, James TC, Sterrit LW (1993) The cryogenic limb array etalon spectrometer (CLAES). J Geophys Res 98(10):10763–10775

Rodgers CD (2000) Inverse methods for atmospheric sounding: theory and practice. World Scientific Publishing Co, River Edge, 238 pp

Rothman LS, Gordon IE, Barbe A, Benner DC, Bernath PF, Birk M, Boudon V, Brown LR, Campargue A, Champion J-P, Chance K, Coudert LH, Dana V, Devi VM, Fally S, Flaud J-M, Gamache RR, Goldman A, Jacquemart D, Kleiner I, Lacome N, Lafferty WJ, Mandin J-Y, Massie ST, Mikhailenko ST, Miller CE, Moazzen-Ahmadi N, Naumenko OV, Nikitin AV, Orphal J, Perevalov VI, Perrin A, Predoi-Cross A, Rinsland CP, Rotger M, Šimečková M, Smith MAH, Sung K, Tashkun SA, Tennyson J, Toth RA, Vandaele AC, Vander Auwera J (2009) The HITRAN 2008 molecular spectroscopic database. J Quant Spectrosc Radiat Transf 110:533–572

Russell JM III, Gordley LL, Park JH, Drayson SR, Hesketh DH, Cicerone RJ, Tuck AF, Frederick JE, Harries JE, Crutzen PJ (1993) The halogen occultation experiment. J Geophys Res 98(D6):10777–10797

Russell JM III, Mlynczak MG, Gordley LL, Tansock JJ, Esplin R (1999) Overview of the SABER experiment and preliminary calibration results. Proc SPIE, Opt Spectr Tech Instrum Atmos Space Res III 3756:277–288

Russell JM III, Bailey SM, Horanyi M, Gordley LL, Rusch DW, Hervig ME, Thomas GE, Randall CE, Siskind DE, Stevens MH, Summers ME, Taylor MI, Englert CR, Espy PJ, McClintock WE, Merkel AW (2009) Aeronomy of ice in the mesosphere (AIM): overview and early science result. J Atmos Sol Terr Phys 79:289–299. doi:10.1016/JjastP2008.08.011

Rybicki GB, Hummer DG (1991) An accelerated lambda iteration method for multilevel radiative transfer. I—Non-overlapping lines with background continuum. Astron Astrophys 245:171–181

Rybicki GB, Hummer DG (1992) An accelerated lambda iteration method for multilevel radiative transfer. II—Overlapping transitions with full continuum. Astron Astrophys 262:209–215

Sharma RD (1987) Infrared airglow, progress in atmospheric physics. In: Rodrigo R, López-Moreno JJ, López-Puertas M, Molina A (eds) Proceedings of the 15th annual meeting on atmospheric studies by optical methods. Kluwer, Boston, pp 177–186

Sharma RD, Nadile RM (1981) Carbon dioxide (v2) radiance results using a new nonequilibrium model, presented at 19th aerospace sciences meeting, Am Inst Aeronaut Astronaut, St Louis MO, Jan 12–15

Sharma RD, Wintersteiner PP (1990) Role of carbon dioxide in cooling planetary thermospheres. Geophys Res Lett 17:2201–2204

Sharma R, Zygelman B, von Esse F, Dalgarno A (1994) On the relationship between the population of the fine structure levels of the ground electronic state of atomic oxygen and the translational temperature. Geophys Res Lett 21:1731–1734

She C-Y, Vance JD, Williams BP, Krueger DA, Moosmüller H, Gibson-Wilde D, Fritts D (2002) Lidar studies of atmospheric dynamics near polar mesopause. EOS Trans AGU 83(27):289–293

She C-Y, Sherman YJ, Yuan T, Williams BP, Arnold K, Kawahara TD, Li T, Xu LF, Vance JD, Acott P, Krueger DA (2003) The first 80-hour continuous lidar campaign for simultaneous observation of mesopause region temperature and wind. Geophys Res Lett 30:1319–1323. doi:10.1029/2002GL016412

Shved GM, Khvorostovskaya LE, Potekhin IYu, Demyanikov AI, Kutepov AA, Fomichev VI (1991) Measurement of the quenching rate constant for collisions $CO_2(0110)$–O: the importance of the rate constant magnitude for the thermal regime and radiation of the lower thermosphere. Izvest Atmos Ocean Phys 27:431–437

Shved GM, Kutepov AA, Ogibalov VP (1998) Non-local thermodynamic equilibrium in CO_2 in the middle atmosphere. I. Input data and populations of the v_3 mode manifold states. J Atmos Sol Terr Phys 60:289–314

Smith WL (1970) Iterative solution of the radiative transfer equation for the temperature and absorbing gas profile of an atmosphere. Appl Opt 9:1993–1999

Smith AK (2012) Global dynamics of the MLT. Surv Geophys. doi:10.1007/s10712-012-9196-9

Smith AK, Marsh DR, Mlynczak MG, Mast JC (2010) Temporal variations of atomic oxygen in the upper mesosphere from SABER. J Geophys Res 115:D18309–D18326. doi:10.1029/2009JD013434

Sonnemann GR, Grygalashvyly M, Berger U (2005) Autocatalytic water vapor production as a source of large mixing ratios within the middle to upper mesosphere. J Geophys Res 110:D1530310. doi:10.1029/2004JD005593

Stair AT Jr, Sharma RD, Nadile RM, Baker DJ, Grieder WF (1985) Observations of limb radiance with cryogenic spectral infrared rocket experiment. J Geophys Res 90(A10):9763–9775

Taylor R (1974) Energy transfer processes in the stratosphere. Can J Chem 52:1436–1451

Taylor FW, Rodgers CD, Whitney JG, Werrett ST, Barnett JJ, Peskett GD, Venters P, Ballard J, Palmer CWP, Knight RJ, Morris P, Nightingale T, Dudhia A (1993) Remote sensing of the atmospheric structure and composition by pressure modulator radiometry from space: the ISAMS experiment on UARS. J Geophys Res 98(D6):10799–10814. doi:10.1029/92JD03029

Thomas G (2003) Are noctilucent clouds harbingers of global change in the middle atmosphere? Adv Space Res 32(9):1737–1746

Thomas RJ, Barth CA, Rusch DW, Sanders RW (1984) Solar mesosphere explorer near-infrared spectrometer: measurements of 1.27 μm radiances and the interference of mesospheric ozone. J Geophys Res 89:9569–9580

Unsöld A (1968) Physik der Sternatmospharen, Springer-Verlag Berlin, Heidelberg, New York, 866 pp

Vollmann K, Grossmann KU (1997) Excitation of 4.3 μm CO_2 emissions by O(^{1}D) during twilight. Adv Space Res 20(6):1185–1189

Weitkamp C (2005) Lidar, range-resolved optical remote sensing of the atmosphere. Springer, New York

Whiteway JA, Carswell AI (1995) Lidar observations of gravity wave activity in the upper stratosphere over Toronto. J Geophys Res 100:14113–14124

Wintersteiner PP, Picard RH, Sharma RD, Winick JR, Joseph RA (1992) Line-by-line radiative excitation model for the non-equilibrium atmosphere: application to CO_2 15 μm emission. J Geophys Res D 97:18083–18117

Yankovsky VA, Babaev AS (2010) Specified calculation of the distribution of molecules of O_2 (X, v = 1–30) in the mesosphere using new data on the quenching rate constant of reaction O_2(X, v) with atomic oxygen. Atmos Ocean Opt 23(8):640–649 (in Russian)

Yankovsky VA, Manuilova RO (2006) Model of daytime emissions of electronically-vibrationally excited products of O_3 and O_2 photolysis: application to ozone retrieval. Ann Geophys 24(11):2823–2839

Yankovsky V, Manuilova R, Babaev A, Feofilov A, Kutepov A (2011) Model of electronic-vibrational kinetics of the O_3 and O_2 photolysis products in the middle atmosphere: applications to water vapor

retrievals from SABER/TIMED 6.3 μm radiance measurements. Int J Rem Sens, "Atmospheric studies by optical methods 36AM" special issue, pp 3065–3078

Yee J-H, Cameron GE, Kusnierkiewicz DY (1999) Overview of TIMED. SPIE 3756:244–254

Zaragoza G, López-Puertas M, López-Valverde MA, Taylor FW (2000) Global distribution of CO_2 in the upper mesosphere as derived from UARS/ISAMS measurements. J Geophys Res 105(19829). doi: 10.1029/2000JD900243